LAWRENCE
LIVERMORE
NATIONAL
LABORATORY

UCRL-TR-217327

Localized Corrosion of Alloy 22

-Fabrication Effects-

FY05 SUMMARY REPORT

R. B. Rebak

Yucca Mountain Project
Lawrence Livermore National Laboratory

September 2005

[1] Corresponding author: rebak1@llnl.gov, raul_rebak@ymp.gov

Auspices
This work was performed under the auspices of the U.S. Department of Energy by University of California, Lawrence Livermore National Laboratory under Contract W-7405-Eng-48.

EXECUTIVE SUMMARY

This report deals with the impact of fabrication processes on the localized corrosion behavior of Alloy 22 (N06022). The four fabrication processes that were analyzed are: (1) Surface stress mitigation of final closure weld, (2) Manufacturing of the mockup container, (3) Black annealing of the container and (4) Use of different heats of Alloy 22 for container fabrication.

Immersion and Electrochemical tests performed in the laboratory are generally aggressive and do not represent actual repository environments in Yucca Mountain. For example, to determine the intergranular attack in the heat affected zone of a weldment, tests are conducted in boiling acidic and oxidizing solutions according to ASTM standards. These solutions are used to compare the behavior of differently treated metallic coupons. Similarly for electrochemical tests many times pure sodium chloride or calcium chloride solutions are used. Pure chloride solutions are not representative of the repository environment.

1. Surface Stress Mitigation: When metallic plates are welded, for example using the Gas Tungsten Arc Welding (GTAW) method, residual tensile stresses may develop in the vicinity of the weld seam. Processes such as Low Plasticity Burnishing (LPB) and Laser Shock Peening (LSP) could be applied locally to eliminate the residual stresses produced by welding. In this study, Alloy 22 plates were welded and then the above-mentioned surface treatments were applied to eliminate the residual tensile stresses. The aim of the current study was to comparatively test the corrosion behavior of as-welded (ASW) plates with the corrosion behavior of plates with stress mitigated surfaces. Immersion and electrochemical tests were performed. Results from both immersion and electrochemical corrosion tests show that the corrosion resistance of the mitigated plates was not affected by the surface treatments applied.

2. Behavior of Specimens from a Mockup container: Alloy 22 has been extensively tested for general and localized corrosion behavior both in the wrought and annealed condition and in the as-welded condition. The specimens for testing were mostly prepared from flat plates of material. It was important to determine if the process of fabricating a full diameter Alloy 22 container will affect the corrosion performance of this alloy. Specimens were prepared directly from a fabricated container and tested for corrosion resistance. Results show that both the anodic corrosion behavior and the localized corrosion resistance of specimens prepared from a welded fabricated container were the same as from flat welded plates. That is, rolling and welding plates using industrial practices do not hinder the corrosion resistant of Alloy 22.

3. Effect of Black Annealing Oxide Scale: The resistance of Alloy 22 to localized corrosion, mainly crevice corrosion, has been extensively investigated in the last few years. This was done mostly using freshly polished specimens. At this time it was important to address the effect an oxide film or scale that forms during the high temperature annealing process or solution heat treatment (SHT) and its subsequent water quenching. Electrochemical tests such as cyclic potentiodynamic polarization (CPP) have been carried out to determine the repassivation potential for localized corrosion and to assess the mode of attack on the specimens. Tests have been carried out in parallel using mill annealed (MA) specimens free from oxide on the surface. The comparative testing was carried out in six different electrolyte solutions at temperatures

ranging from 60°C to 100°. Results show that the repassivation potential of the specimens containing the black anneal oxide film on the surface was practically the same as the repassivation potential for oxide-free specimens.

4. Heat-to-Heat Variability – Testing of Ni-Cr-Mo Plates with varying heat chemistry: The ASTM standard B 575 provides the range of the chemical composition of Nickel-Chromium-Molybdenum (Ni-Cr-Mo) alloys such as Alloy 22 (N06022) and Alloy 686 (N06686). For example, the content of Mo is specified from 12.5 to 14.5 weight percent for Alloy 22 and from 15.0 to 17.0 weight percent for Alloy 686. It was important to determine how the corrosion rate of welded plates of Alloy 22 using Alloy 686 weld filler metal would change if heats of these alloys were prepared using several variations in the composition of the elements even though still in the range specified in B 575. All the material used in this report were especially prepared at Allegheny Ludlum Co. Seven heats of plate were welded with seven heats of wire. Immersion corrosion tests were conducted in a boiling solution of sulfuric acid plus ferric sulfate (ASTM G 28 A) using both as-welded (ASW) coupons and solution heat-treated (SHT) coupons. Results show that the corrosion rate was not affected by the chemistry of the materials within the range of the standards.

In short, this report shows that the corrosion behavior of Alloy 22 is not affected by fabrication processes such a cold rolling and welding, air solution heat-treating and surface stress mitigation. The report also shows that as long as Alloy 22 is produced within the range of composition specified in ASTM B 575, the corrosion resistance of one heat of material would be undistinguishable from the corrosion resistance of another heat of material.

1. Introduction

This report analyzes localized corrosion data for Alloy 22 that was gathered during FY04 and FY05 and that was examined during FY05. Table 1.1 shows the packages of data in TDMS and the respective DTN numbers that are discussed in this report. This report deals mainly with issues related to the fabrication of the container and the impact on the resistance to localized corrosion of Alloy 22. Table 1.2 shows data packages that will be part of future reports.

Table 1.1 – List of DTN with data analyzed in this report.

DTN number	Title	Report Section
LL040905212251.120	Effect of Annealing and Air-Formed Films on Critical Potential	4
LL050501012251.033	Repassivation Potentials for Alloy 22 with Annealed Air Formed Oxide Films (Black Annealing)	4
LL050502412251.144	Repassivation Potentials for Alloy 22 with Annealed Air Formed Oxide Films (Black Annealing) – Part II.	4
LL050600812251.146	Immersion Corrosion Tests of Burnished, Laser Peened and As-Welded Alloy 22 Welded Plates	2
LL040706812251.114	Crevice Corrosion Study by Cyclic Polarization Technique of Laser Peened, Burnished and As-Welded Alloy 22 Specimens	2
LL040902712251.119	Corrosion Rate and Potential Parameter Data Taken from Cyclic Potentiodynamic Polarization (CPP) Curves for Laser Peened, Burnished and As-Welded Alloy 22 Specimens	2
LL050302312251.129	Electrochemical Behavior of Alloy 22 Specimens Prepared from a Mockup Container	3
LL050502512251.145	Immersion Corrosion Tests of Heat to Heat Variability in Ni-Cr-Mo Alloys	5

Table 1.2 – List of data packages to be analyzed in future reports

Order	Description of Data Package
1.	Comparison between the repassivation potential for Alloy 22 from Cyclic Potentiodynamic Polarization (CPP) and the Tsujikawa Hisamatsu Electrochemical (THE) method both for pure chloride solutions and solutions containing chloride and nitrate
2.	Localized corrosion behavior of Alloy 22 between 120°C and 160°C in high concentration chloride and chloride plus nitrate brines using CPP, constant potentials and immersion at the free corrosion potential tests.
3.	Effect of the long term immersion of welded and non-welded Alloy 22 on the anodic behavior in chloride and chloride plus nitrate solutions
4.	Comparison of the repassivation potential of welded and non-welded Alloy 22

2. Effect of Surface Stress Mitigation

2.1. Introduction

The effect of surface stress mitigation was studied under the FY04 technical work plan (TWP) AWPT25. Testing was directed by John C. Estill and Tammy Summers. Immersion tests were carried out by David V. Fix and the electrochemical tests were carried out by Ahmet Yilmaz. Scanning electron microscope images are by Lana L. Wong. The experimental details of this work are documented in SN-LLNL-SCI-483-V1 pp. 1 – 76 for the immersion tests and in SN-LLNL-SCI-471-V2 pp. 92-130 for the electrochemical tests. The data is in TDMS under DTN LL040902712251.119 and DTN LL040706812251.114 for the electrochemical tests and DTN LL050600812251.146 for the immersion tests.

Alloy 22 (N06022) has nominally 56% Nickel (Ni), 22% Chromium, 13% Molybdenum (Mo) and 3% Tungsten (W). [1] Alloy 22 is highly resistant to all types of corrosion, including environmentally assisted cracking, localized corrosion such as crevice corrosion and general or uniform corrosion. [2-4] Alloy 22 was selected for the fabrication of the outer shell of the high level nuclear waste containers for the proposed Yucca Mountain repository. [5-6] The containers will be fabricated and solution heat-treated before the waste is loaded into the containers. [6] After loading, the closure lid of the Alloy 22 containers will be welded using the gas tungsten arc welding (GTAW) process. [7] There are currently two methods under consideration to minimize or eliminate residual tensile stresses that may result from the final closure welding. These are: (1) Low Plasticity Burnishing (LPB) and (2) Laser shock Peening (LSP). These stress mitigation treatments are aimed to reducing residual surface tensile stresses that could promote the initiation of environmentally assisted cracking (EAC) in Alloy 22. [6]

It is important to know if the proposed surface treatments will affect the general and localized corrosion resistance of welded plates. The aim of this work was to compare the general and localized corrosion resistance of Alloy 22 in as-welded (ASW) plates and in welded plates that were treated for surface stress mitigation. Immersion and electrochemical tests were performed to assess changes in the corrosion resistance of the three studied materials.

Keywords: N06022, Corrosion Rate, Crevice Corrosion, Gas Tungsten Arc Welding, Stress Mitigation, Burnishing, Laser Peening

2.2. Experimental

Coupons and specimens were prepared from three differently treated welded plates of Alloy 22. Both immersion and electrochemical tests were conducted following ASTM standards. [8]

2.2.1. As-Welded (ASW) Plates

Two 1-inch thick Alloy 22 plates (Heat XX2246BG) were GTAW welded lengthwise using 0.045-inch thick Alloy 22 wire (XX2048BG) for filler metal. Before the weld joining, each plate was approximately 16-inch long and 6-inch wide. The ASW plate used for corrosion testing

was called F6 and the coupons and specimens prepared from this plate were all named starting with the letter W.

2.2.2. Low Plasticity Burnishing (LPB)

LPB is a process by which a smooth hard ball is rolled over the surface of the metal to be burnished imparting compressive deformation. [9-10] The treatment in the studied Alloy 22 welded plates was performed in two steps using balls of two different sizes, the larger one with an effective surface area of 0.0154 inch² and the smaller one with an effective surface area of 0.00067 inch². In the first step the larger ball was rolled at a pressure of 780 ksi to create compressive stresses to a larger depth. In the second step, the smaller ball was rolled at a pressure of 821 ksi to increase the level of compressive stresses near the surface. The LPB treatment of the Alloy 22 studied plates was carried out at the Surface Enhancement Technologies Company in Cincinnati, Ohio. The burnished plate was called F4 and the coupons and specimens prepared from this plate were all named starting with the letter B.

2.2.3. Laser Shock Peening (LSP)

Laser shock peening is a process by which a laser beam is pulsed upon a metallic surface producing a planar shockwave that travels though the work piece and plastically deforms into compressive stresses a layer of material. [11-12] The laser beam is generally applied to the work piece though a transparent overlay and an absorbent coating. A plasma forms under the overlay increasing the pressure and therefore the compressive stresses on the treated part. It has been shown specifically that a LSP treatment of 33-mm thick Alloy 22 welds actually produced a 4-mm deep layer of compressive stresses on the surface. [12] The current LSP treatment in the Alloy 22 welded plates was performed by applying laser pulses of 14 Joules for 25 nano seconds. Each spot dimension was approximately 2.5 mm square. The laser-peened plate was called F2 and the coupons and specimens prepared from this plate were all named starting with the letter P.

2.2.4. Preparation of the Immersion Coupons

Three types of welded plates were studied: (1) As-Welded (ASW), (2) Welded plus LPB and (3) Welded plus LSP. Table 2.1 shows the heat numbers and the chemical composition of the plates. The plates met the specifications of ASTM B 575. [1] The plates were cut in approximately 0.5-inch thick slices perpendicular to the weld seam. There were two LPB plate slices (B9 and B10), three LSP plate slices (P13, P14 and P15) and three ASW plate slices (W13, W14 and W15). The immersion corrosion testing coupons were prepared from the above listed plate slices. The testing coupons were approximately 0.5 to 1-inch wide, 0.25 to 0.5-inch thick and 2-inch long. The 2-inch length contained the weld seam at the center and base metal at both sides of the weld seam. These sizes were constrained by the testing apparatus (ASTM G 28). [8] The surface area of the coupons varied generally from 20 to 40 cm² and the weight varied from 40 to 90 g. The coupons were degreased in acetone, rinsed in de-ionized water and let dry. Each coupon was dimensioned and weighed three times before the corrosion testing started.

2.2.5. ASTM G 28 A or Ferric Sulfate + Sulfuric Acid Test

This method measures the susceptibility of nickel alloys to intergranular attack. It is often used to determine preferential intergranular attack near welds or in heat affected zones (HAZ). The guidelines are specified in the Annual Book of ASTM standards. [8] Figure 2.1 shows the setting for the tests. The ASTM G 28 A method for Alloy 22 consists in immersing coupons of the alloy for 24 h in a boiling solution of 42 g/L $Fe_2(SO_4)_3$ (ferric sulfate) plus 50% H_2SO_4 (sulfuric acid). The difference in the mass of the coupon between before and after the test can be used to calculate the uniform corrosion rate. Corrosion rates were calculated according to Equation 2.1 [8]

$$CR(mm/year) = 8.76 \times 10^4 \frac{\Delta W(g)}{A(cm^2) \cdot t(h) \cdot d(g \cdot cm^{-3})} \qquad (2.1)$$

Where ΔW is the difference if weight (mass) of the coupon between before and after the test, A is the surface area of the coupon, t is the testing time (24 h) and d is the density of Alloy 22 (8.69 g/cm³). [8]

The testing coupons were parallelepipeds, that is, they had six faces. Only one face is of interest (the treated one, which was either ASW, LPB or LSP). The other faces are as-cut faces and remained in the same condition for all three types of coupons. Whenever comparing surface characteristics after corrosion only the face of interest is discussed. Figure 2.2 shows the general appearance of three coupons after immersion testing. These coupons represent each one of the testing materials.

2.2.6. Preparation of the Electrochemical Specimens

Alloy 22 specimens were mainly prepared from 1-inch thick plate. Table 2.1 gives the heats and the chemical composition of the material for the tested specimens. The specimens were prism crevice assemblies (PCA) (Figure 2.3) as reported elsewhere. [13] For the current tests, the surface area of the PCA specimens was 3.27 cm². The original surface of a PCA specimen is usually 14.06 cm². [13] However for the current specimens, all the non-important surfaces were lacquered to avoid their interaction with the environment. Thus, only the ASW, LPB and LSP surfaces were exposed to the electrolyte solution for the tests. The crevicing mechanism for these PCA tests was based on ASTM G 48 12-tooth washer; however the washer was not the standard ceramic plus PTFE tape used in other tests at LLNL. [13] Since the current specimens did not have a completely smooth flat surface the crevicing washer was constructed using a hard organic material (PVDF or Polyvinylidene fluoride), which could sufficiently deform and provide a tight crevicing mechanism on an uneven surface. The PVDF washers were also coated with PTFE tape in a similar way as the ceramic washers. The PCA specimens were degreased in acetone and DI water, let dry and then all the non-important surfaces were lacquered. The lacquer was allowed to dry for at least 6 hours and then the specimens were inspected for discontinuities. The resistance of the lacquered surfaces was measured to verify electrical insulation from the electrolyte. The specimens were also inspected after the tests confirming that the lacquer did not

break or disbond during testing. Specimens were used in the as-welded (ASW), in the low plasticity burnishing (LPB) and in the laser shock peened (LSP) conditions. The specimens were labeled respectively W, B and P. The weld seam run across center of the surface of the specimen that was purposely creviced with the multiple teeth washer (Figure 2.3).

2.2.7. Electrolyte Solutions for Electrochemical Tests and Testing Sequence

Electrochemical tests were performed in deaerated simple salt solutions. These solutions were 1 M NaCl pH 6 at 90°C and 6 m NaCl + 0.9 m KNO_3 pH 5.5 at 80°C and 100°C. The second solution has a $[Cl^-]/[NO_3^-]$ ratio of 6.67. Nitrogen (N_2) was purged through the solution at a flow rate of 100 cc/min for 24 hours while the corrosion potential (E_{corr}) was monitored. Nitrogen bubbling was carried throughout all the electrochemical tests. The electrochemical tests were conducted in a one-liter, three-electrode, borosilicate glass flask (ASTM G 5). [8] A water-cooled condenser combined with a water trap was used to avoid evaporation of the solution and the ingress of air. The temperature of the solution was controlled by immersing the cell in a thermostatisized silicone oil bath. All the tests were carried at ambient pressure. The reference electrode was saturated silver chloride (SSC) electrode, which has a potential of 199 mV more positive than the standard hydrogen electrode (SHE). The reference electrode was connected to the solution through a water-jacketed Luggin probe so that the electrode was maintained at near ambient temperature. The counter electrode was a flag (36 cm^2) of platinum foil spot-welded to a platinum wire. All the potentials in this paper are reported in the SSC scale.

Basically, the test sequence for each specimen consisted of three parts: (1) E_{corr} evolution as a function of time for 24 h, (2) Polarization Resistance (ASTM G 59) three subsequent times and (3) A larger anodic polarization to determine susceptibility to crevice corrosion. The larger anodic polarization was conducted using Cyclic Potentiodynamic Polarization (CPP) method (ASTM G 61).

Polarization Resistance (ASTM G 59)- Corrosion rates (CR) were obtained using the polarization resistance method (ASTM G 59). [8] Each one of these tests lasts approximately four minutes. An initial potential of 20 mV below the corrosion potential (E_{corr}) was ramped to a final potential of 20 mV above E_{corr} at a rate of 0.167 mV/s. Linear fits were constrained to the potential range of 10 mV below E_{corr} to 10 mV above E_{corr}. During the fitting of the data to calculate the polarization resistance (Rp), the potential (E) was plotted in the X-axis. The Tafel constants, b_a and b_c, were assumed to be $\pm$ 0.12 V/decade. Corrosion rates were calculated using Equation 2.2

$$i_{corr} = \frac{1}{R_p} \times \frac{b_a \cdot b_c}{2.303(b_a + b_c)} \Leftrightarrow and \Leftrightarrow CR(\mu m / yr) = k \frac{i_{corr}}{\rho} EW \qquad (2.2)$$

Where k is a conversion factor (3.27 x 10^9 $nm \cdot g \cdot A^{-1} \cdot cm^{-1} \cdot yr^{-1}$), i_{corr} is the corrosion current density in A/cm^2 (calculated from the measurements of the resistance to polarization, R_p), EW is the equivalent weight, and ρ is the density of Alloy 22 (8.69 g/cm^3). Assuming an equivalent dissolution of the major alloying elements as Ni^{2+}, Cr^{3+}, Mo^{6+}, Fe^{2+}, and W^{6+}, the EW for Alloy 22 is 23.28 (ASTM G 102). [8]

Cyclic Potentiodynamic Polarization - CPP (ASTM G 61)- The test to assess the susceptibility of Alloy 22 to localized corrosion and passive stability was the cyclic potentiodynamic polarization technique, CPP (ASTM G 61). [8] The potential scan was started 100 mV below E_{corr} at a set scan rate of 0.167 mV/s. The scan direction was reversed when the current density reached 5 mA/cm^2 in the forward scan. Depending on the range of applied potentials, each CPP test could last between 1 h and 3 h. From the polarization curve, several parameters of importance can be extracted. The E20 and E200 represent values of breakdown potential and ER10, ER1 and ERCO represent values of repassivation potential.

2.3. Results

2.3.1. Immersion Corrosion Tests

Table 2.2 shows the corrosion rate results from the immersion testing. For all three types of coupons (ASW, LPB and LSP) the corrosion rate was the same. The highest average corrosion rate corresponded to the ASW coupons and the lowest to the LSP coupons but considering the standard deviation (SD), the corrosion rate values are indistinguishable from each other. Besides the data reported on Table 2.2, the corrosion rate of the base metal of the plates (away from the weld) in ASTM G 28 was also measured. The corrosion rate of the base metal was found to be 1.83 mm/year, which was higher than that of any of the welded coupons. It has been previously reported that the corrosion rate of as-welded 0.125-inch thick sheets of Alloy 22 in ASTM G 28A was 1.08 mm/year. [14] The standard corrosion rate of Alloy 22 given in a commercial brochure is 1.016 mm/year. [2] The common acceptance criterion for the maximum allowed corrosion rate for Alloy 22 is 80 mpy or 2 mm/year. [15]

After the corrosion immersion tests each specimen was thoroughly inspected under optical microscopy (stereomicroscope). Results are given in Table 2.3. All three type of materials suffered intergranular attack (IGA) in the heat affected zone (HAZ). Figure 2.2 shows macrograph images of characteristic tested coupons. The obvious IGA in the HAZ appears as black strips on each side of the weld seam (Figure 2.2). The IGA in the HAZ seemed less defined in the LSP (Figure 2.2c) coupons than in the ASW coupons (Fig. 2.2a).

Figures 2.4 and 2.5 show the aspect of the ASW corroded coupons, in the base metal part of it. Figure 2.4 represents the base metal away from the weld seam, which is the part of the plate that was not affected by the welding process. Figure 2.4 shows shallow and sporadic IGA. Figure 2.5 shows the aspect of corrosion in the HAZ, which is a couple of millimeters from the edge of the weld seam. Figure 2.5 shows more pronounced IGA probably promoted by second phase precipitation due to the exposure of the HAZ to intermediate temperatures (600 to 900°C) for the time involved in the welding process. [14-15]

Figures 2.6 and 2.7 show the aspect of the LPB corroded coupons, in the base metal part of it. Figure 2.6 represents the base metal away from the weld seam, which is the part of the plate that was not affected by the welding process. Figure 2.6 shows shallow and sporadic IGA, the same as in the ASW coupon (Figure 2.4). Figure 2.7 shows the aspect of corrosion in the HAZ, which is a couple of millimeters from the weld seam. Figure 2.7 shows more pronounced IGA than in the base metal away from the weld. This was probably promoted by second phase

precipitation due to the exposure of the HAZ to intermediate temperatures (600 to 900°C) for the time involved in the welding process. [14-15] The aspect of Figure 2.7 is similar to that of Figure 2.5 showing that LPB treatment did not decrease the corrosion characteristics of an untreated welded plate (ASW).

Figures 2.8 and 2.9 show the LSP corroded coupons in the base metal part. Figure 2.8 represents the base metal away from the weld seam, which is the part of the plate that was not affected by the welding process. Figure 2.8 shows shallow and sporadic IGA, the same as in the ASW and LPB coupons (Figures 2.4 and 2.6). Figure 2.9 shows the corrosion in the HAZ, which is a couple of millimeters from the edge of the weld seam. Figure 2.9 shows a type of attack that is less pronounced IGA and more type of enhanced general corrosion. It appears that the localized corrosion in the HAZ was different in the LSP coupon (Figure 2.9) than in the ASW and LPB coupons (Figures 2.5 and 2.7). At this moment it cannot be speculated what mechanism could have changed the mode of attack of the LSP coupons.

2.3.2. Electrochemical Tests

The 24-h Corrosion Potential

Table 2.3 shows the average E_{corr} for the three types of material after 24-hour immersion in deaerated 1 M NaCl at 90°C. The corrosion potentials in Table 2.3 do not represent the long-term steady state potential that the alloy may adopt in aerated environments. Table 2.3 shows that the E_{corr} in pure chloride solutions was the same for all three materials ASW, LPB and LSP. Table 2.4 lists the average E_{corr} values in deaerated 6 m NaCl + 0.9 m KNO_3 at 80°C and 100°C. For the LPB specimens only data at 100°C is available due to the limited number of specimens available for testing. For both the ASW and LSP specimens, as the temperature increased from 80°C to 100°C, the E_{corr} slightly decreased. This is expected since at higher temperatures metals tend to become more active in saline solutions. Table 2.4 also shows that at 100°C the E_{corr} of all three materials (ASW, LPB and LSP) was the practically same and between –238 mV and –272 mV SSC, showing that the three materials behaved similarly when immersed for 24-h in hot saline solutions.

The Corrosion Rate from R_p Measurements

Tables 2.3 and 2.4 show the corrosion rates of all three tested materials (ASW, LPB and LSP) in deaerated 1 M NaCl and in 6 m NaCl + 0.9 m KNO_3 solutions, respectively. The corrosion rates in Tables 2.3 and 2.4 do not represent the long-term steady state corrosion rate that the alloy may adopt in an aerated environment. Table 2.3 shows that the average corrosion rate of all the tested material in 1 M NaCl solution varied between 0.188 μm/year for the LPB specimens and 0.330 μm/year for the LSP specimens. The LSP average corrosion rate was the highest due to the abnormally high corrosion rate values of specimen P2. Considering standard deviations, the corrosion rate values for ASW, LPB and LSP cannot be differentiated from each other (Table 2.3).

Table 2.4 shows the average corrosion rates for the three materials in 6 m NaCl + 0.9 m KNO_3 at 80°C and 100°C. The effect of the temperature on the corrosion rate cannot be fully

quantified since there are specimens that gave corrosion rates that may be result of anomalous behavior (e.g. W3, W4 and P3). It is likely that for longer immersion times, when steady state conditions are achieved, the corrosion rates for the three materials will tend to converge. Nevertheless, in spite of the short immersion time, the corrosion rate of the three materials at 100°C (ignoring the anomalous behaviors) fluctuated between 0.18 μm/year for LSP and 0.21 μm/year for the ASW specimens. These values can be considered practically the same. That is, in both electrolyte solutions all materials behaved the same regarding corrosion rate measures using ASTM G 59.

Cyclic Potentiodynamic Polarization (CPP)

Figure 2.10 shows the cyclic potentiodynamic polarization curves for the three tested materials in deaerated 1 M NaCl pH 6 at 90°C. Figure 2.10 shows that the behavior of all these materials was practically the same. Similarly, Figure 2.11 shows the cyclic potentiodynamic polarization curves for the three tested materials in deaerated 6 m NaCl + 0.9 m KNO_3 pH 5.5 at 100°C. Again, the polarization curves are the same for the ASW, LPB and LSP materials in the chloride plus nitrate brine.

Table 2.4 shows the effect of the temperature on the breakdown and repassivation potential for ASW and LSP materials (LPB was not tested at 80°C). As the temperature increased from 80°C to 100°C, both the breakdown and repassivation potentials slightly decreased as it may be expected.

Figures 2.12 and 2.13 show E_{corr} and the parameters from the CPP curves (listed in Tables 2.3 and 2.4) for 1 M NaCl at 90°C and for 6 m NaCl + 0.9 m KNO_3 at 100°C, respectively. For the 1 M NaCl solution (Table 2.3 and Figure 2.12), the breakdown potentials (E20 and E200) seemed slightly higher for LPB than for ASW and LSP materials. However, the repassivation potentials (ER1 and ERCO) seemed higher for the ASW material. In the 6 m NaCl + 0.9 m KNO_3 solution (Table 2.4 and Figure 2.13), the breakdown potentials (E20 and E200) seemed slightly higher for LPB than for ASW and LSP. However, the repassivation potentials (ER1 and ERCO) seemed higher for the LSP material. The difference in potential values between the three materials is small enough to be considered within experimental error. For example, in the 6 m NaCl + 0.9 m KNO_3 solution at 100°C, the difference between the values of E200 is smaller than 10 mV between one type of material and another (Table 2.4).

Figures 2.14 through 2.19 show that the mode of crevice corrosion attack 1 M NaCl at 90°C does not change if the ASW plate is LPB or LSP treated. When creviced Alloy 22 is polarized to high anodic potentials (Figure 2.10) the specimens may suffer crevice corrosion. Figures 2.14 and 2.15 show the mode of crevice corrosion attack in ASW specimen W6. This is a typical type of crevice corrosion for Alloy 22 in 1 M NaCl at 90°C solution. [13] Figure 2.14 also shows that the ASW specimen was not totally flat since it was not finished with 600 grit paper as in previous tests. [13] Figure 2.15 shows a detail of the crevice corrosion attack in Figure 2.14, where a characteristic dendritic structure of the weld seam can be seen. Similar findings are for LPB specimen B3 (Figures 2.16 and 2.17) and for LSP specimen P5 (Figures 2.18 and 2.19).

Table 2.5 compares data in Tables 2.3 and 2.4 with data known from previous publications for other tested Alloy 22 specimens in the same electrolytes. In spite that the referenced data [13,16] was developed for freshly ground paper 600 and fully exposed (not lacquered) creviced specimens, the repassivation potentials in each environment (pure chloride

and chloride plus nitrate) are practically the same. This observation (Table 2.5) not only demonstrates that stress mitigated materials behave electrochemically the same as as-welded materials but also gives confidence that the testing methods used here provide accurate and reproducible parameters to compare the behavior of different materials.

2.4. Conclusions

(1) Surface tensile stress mitigation processes such as low plasticity burnishing (LPB) and laser shock peening (LSP) do not affect the corrosion resistance of welded Alloy 22 plates.

(2) Immersion tests in standard G 28 A solution showed that the corrosion rate by weight loss was the same for as-welded (ASW) material as for LPB and LSP materials

(3) Electrochemical tests such as cyclic potentiodynamic polarization showed that the anodic behavior of the three tested materials (ASW, LPB and LSP) was the same

(4) The repassivation potential in chloride solutions of the three materials was the same

(5) When corrosion occurred, the mode of attack of the three materials (ASW, LPB and LSP) remained the same.

2.5. References

1. ASTM International, Annual Book of ASTM Standards, Volume 02.04 "Non-Ferrous Metals" Standard 575 B (West Conshohocken, PA: ASTM International, 2002).
2. Haynes International, "Hastelloy C-22 Alloy", Brochure H-2019E (Haynes International, 1997: Kokomo, IN)
3. R. B. Rebak, in Corrosion and Environmental Degradation, Volume II, p. 69, Wiley-VCH, Weinheim, Germany (2000)
4. R. B. Rebak and P. Crook, *Advanced Materials and Processes*, February 2000
5. Yucca Mountain Science and Engineering Report, U. S. Department of Energy, Office of Civilian Radioactive Waste Management, DOE/RW-0539, Las Vegas, NV, May 2001
6. G. M. Gordon, Corrosion, 58, 811 (2002)
7. S. C. Lu, G. M. Gordon and P. L. Andresen, PVP-Vol. 483, Transportation, Storage and Disposal of Radioactive Materials (American Society of Mechanical Engineers, 2004: New York, NY)
8. ASTM International, Annual Book of ASTM Standards, Volume 03.02 "Wear and Erosion; Metal Corrosion" p. 91 (West Conshohocken, PA: ASTM International, 2004)
9. U.S. Patents 5,826,453 (Oct. 1998), 6,415,486 B1 (Jul. 2002)

10. P. S. Prevéy, R. A. Ravindranath, M. Shepard and T. Gabb "Case Studies of Fatigue Life Improvement Using Low Plasticity Burnishing in Gas Turbine Engine Applications," Proc. Of ASME Turbo Expo 2003, 16-19 June 2003, Atlanta, GA
11. C. S. Montross, T. Wei, L. Ye, G. Clark and Y.-W. Mai "Laser Shock Processing and its Effects on Microstructure and Properties of Metal Alloys: a Review," International Journal of Fatigue, 24, 1021-1036 (2002)
12. M. R. Hill, A. T. DeWald, L. A. Hackel, H.-L. Chen, R. C. Specht and F. B. Harris "Laser Peening Technology," Advanced Materials and Processes, 8, p. 65 (2003)
13. K. J. Evans, A. Yilmaz, S. D. Day, L. L. Wong, J. C. Estill and R. B. Rebak "Comparison of Electrochemical Methods to Determine Crevice Corrosion Repassivation Potential of Alloy 22 in Chloride Solutions," JOM, January 2005 (to be published)
14. R. B. Rebak, T. S. E. Summers, T. Lian, R. M. Carranza, J. R. Dillman, T. Corbin and P. Crook "Effect of Thermal Aging on the Corrosion Behavior of Wrought and Welded Alloy 22," Corrosion/2002, Paper 02542 (NACE International, 2002: Houston, TX)
15. R. B. Rebak, T. S. E. Summers and R. M. Carranza, "Mechanical Properties, Microstructure and Corrosion Performance of C-22 Alloy Aged at 260°C to 800°C, Scientific Basis for Nuclear Waste Management XXIII, Vol. 608, p. 109 (Materials Research Society, 2000: Warrendale, PA)
16. G. O. Ilevbare, K. J. King, S. R. Gordon, H. A. Elayat, G. E. Gdowski and T. S. E. Summers, "Effect of Nitrate on the Repassivation Potential of Alloy 22 in Chloride Containing Solutions," Fall 2004 Meeting of the Electrochemical Society, 0308Oct04, Honolulu, HI (to be published).

Table 2.1
Chemical Composition in wt% of the Studied Materials

Element	Plate or Base Metal Heat XX2246BG	Weld Wire or Filler Metal Heat XX2048BG
Ni	~60	59.4
Cr	20.4	20.48
Mo	13.9	14.21
W	3.3	3.02
Fe	2.3	2.53
Co	0.2	0.02
Mn	0.2	0.2
V	0.01	0.02
Cu	---	0.04

Table 2.2
Results from G 28 A Immersion Corrosion Tests

Material	Coupon ID	Corrosion Rate, mm/year (mpy)	Average CR ± SD mm/year	Observations After the Tests
ASW	W13-S1	1.26 (49.6)	1.303 ± 0.040	IGA in HAZ, uneven attack in BM away from WS
ASW	W14-S1	1.31 (51.48)		
ASW	W15-S1	1.34 (52.72)		
LPB	B9-S2	1.37 (54.02)	1.295 ± 0.106	IGA in HAZ, deformation marks perpendicular to the WS (effect of the ball?)
LPB	B10-S2	1.22 (48.12)		
LSP	P13-S2	1.32 (52.07)	1.257 ± 0.055	IGA in HAZ, uneven attack on base metal lattice marks (effect of the LSP?)
LSP	P14-S2	1.23 (48.41)		
LSP	P15-S2	1.22 (47.86)		

CR = corrosion rate, SD = standard deviation, IGA = intergranular attack, HAZ = heat affected zone, BM = Base Metal, WS = Weld Seam

Table 2.3
Characteristic Potentials (mV, SSC) and Corrosion Rates (μm/year)
of Alloy 22 in deaerated 1 M NaCl solution at 90°C

ID	Material	$E_{corr,}$ 24 h	Corrosion Rate	E20	E200	ER10	ER1	ERCO
W6	ASW	-286	0.22, 0.27, 0.21	374	567	-17	-88	-104
W7	ASW	-198	0.19, 0.15, 0.21	356	547	-17	-79	-91
Ave ± SD	ASW	-242 ± 44	0.208 ± 0.039	365 ± 9	557 ± 10	-17 ± 0	-84 ± 5	-98 ± 7
B3	LPB	-260	0.18, 0.15, 0.20,	480	706	-59	-123	-134
B4	LPB	-258	0.20, 0.21, 0.19	383	623	-10	-95	-111
Ave ± SD	LPB	-259 ± 1	0.188 ± 0.021	432 ± 49	665 ± 42	-35 ± 25	-109 ± 14	-123 ± 12
P2	LSP	-244	0.41, 0.51, 0.38	319	544	-14	-86	-104
P5	LSP	-195	0.22, 0.23, 0.23	381	575	-22	-100	-114
Ave ± SD	LSP	-220 ± 25	0.330 ± 0.121	350 ± 31	560 ± 16	-18 ± 4	-93 ± 7	-109 ± 5

ID = Specimen Identification, The 24-h corrosion potential and the corrosion rates are illustrative values measured after 24-h immersion in deaerated solutions. They do not represent long-term behavior of the alloy under aerated solutions. Ave ± SD = Average value ± standard deviation, E20 and E200 is the potential in the forward scan for which the current density reaches 20 and 200 μA/cm² respectively. ER10 and ER1 is the potential in the reverse scan for which the current density reaches 10 and 1 μA/cm² respectively. ERCO is the potential at which the reverse scan intercepts the forward scan (cross-over potential).

Table 2.4
Characteristic Potentials (mV, SSC) and Corrosion Rate (μm/year)
of Alloy 22 in 6 m NaCl + 0.9 m KNO_3 at 80°C and 100°C

	Material	E_{corr}, 24 h	Corrosion Rate	E20	E200	ER10	ER1	ERCO
W1, 80	ASW	3	0.27, 0.26, 0.23	727	856	85	NA	NA
W3, 80	ASW	-38	0.74, 0.72, 0.75	798	867	285	-65	-31
Ave ± SD	ASW	-18 ± 21	0.495 ± 0.242	763 ± 36	862 ± 6	185 ± 100	-65 ± 0	-31 ± 0
W4, 100	ASW	-297	2.36, 2.1, 1.93	443	840	-26	-83	-83
W5, 100	ASW	-247	0.22, 0.21, 0.21	441	813	-29	-72	-81
Ave ± SD	ASW	-272 ± 25	1.172 ± 0.966	442 ± 1	827 ± 14	-28 ± 2	-78 ± 6	-82 ± 1
B1, 100	LPB	-251	0.19, 0.22, 0.20,	480	811	-35	-83	-19
B2, 100	LPB	-225	0.20, 0.19, 0.20	488	858	-31	-86	-95
Ave ± SD	LPB	-238 ± 13	0.200 ± 0.010	484 ± 4	835 ± 24	-33 ± 2	-85 ± 2	-57 ± 38
P4, 80	LSP	-183	0.14, 0.14, 0.16	659	858	588	-31	-59
P6, 80	LSP	-279	0.11, 0.15, 0.11	676	874	207	-14	-38
Ave ± SD	LSP	-231 ± 48	0.135 ± 0.019	668 ± 9	866 ± 8	398 ± 191	-23 ± 9	-49 ± 11
P1, 100	LSP	-265	0.17, 0.18, 0.19	443	827	-5	-68	-79
P3, 100	LSP	-248	0.52, 0.39, 0.86	436	830	-19	-77	-45
Ave ± SD	LSP	-257 ± 9	0.385 ± 0.248	440 ± 4	829 ± 2	-12 ± 7	-73 ± 5	-62 ± 17

ID = Specimen Identification, T = Temperature in °C, The 24-h corrosion potential and the corrosion rates are illustrative values measured after 24-h immersion in deaerated solutions. They do not represent long-term behavior of the alloy under aerated solutions. Ave ± SD = Average value ± standard deviation, E20 and E200 is the potential in the forward scan for which the current density reaches 20 and 200 μA/cm² respectively. ER10 and ER1 is the potential in the reverse scan for which the current density reaches 10 and 1 μA/cm² respectively. ERCO is the potential at which the reverse scan intercepts the forward scan (cross-over potential), NA = Not Available.

Table 2.5

Comparison between the Average Characteristic Potentials
of Current Results and Archive Results for N06022

Material/ Data Source	ER1	ERCO	ER, CREV
1 M NaCl, 90°C			
ASW Current	-84 ± 5	-98 ± 7	NA
LPB Current	-109 ± 14	-123 ± 12	NA
LSP Current	-93 ± 7	-109 ± 5	NA
Archive MA MCA Ref. 13	-80 ± 19	-49 ± 16	-30 ± 8
Archive ASW MCA Ref. 13	NA	NA	-99 ± 9
6 m NaCl + 0.9 m KNO_3, 100°C			
ASW Current	-78 ± 6	-82 ± 1	NA
LPB Current	-85 ± 2	-57 ± 38	NA
LSP Current	-73 ± 5	-62 ± 17	NA
Archive ASW MCA Ref. 16	-49 ± 27	-63 ± 23	NA
MCA = Multiple Crevice Assembly (lollipop), ER,CREV obtained using the Tsujikawa-Hisamatsu Electrochemical (THE) Method			

Figure 2.1 - Setting for the ASTM G 28 A tests.

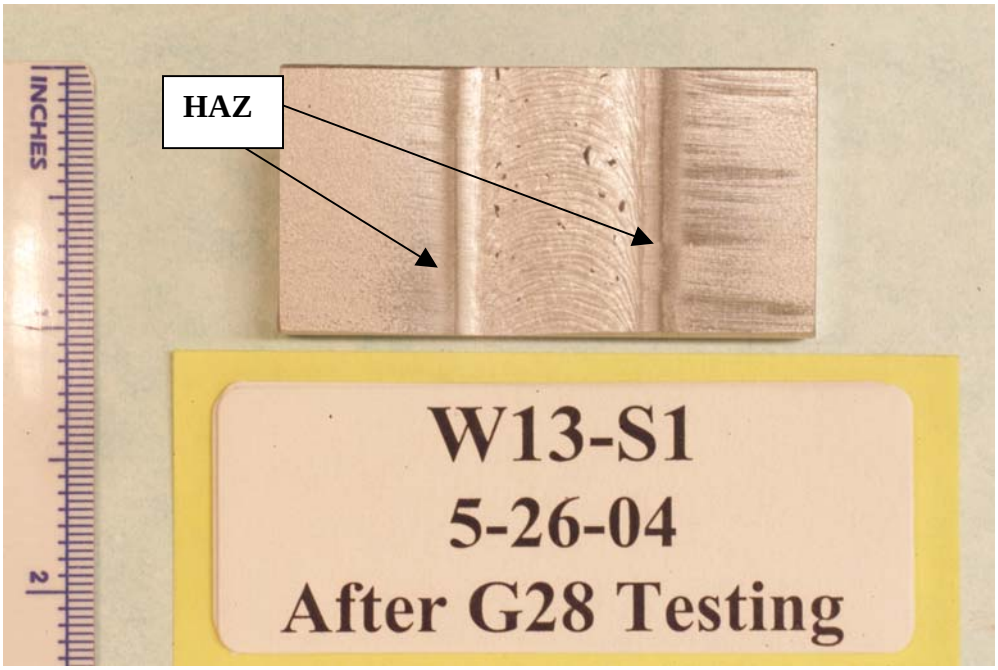

Figure 2.2a

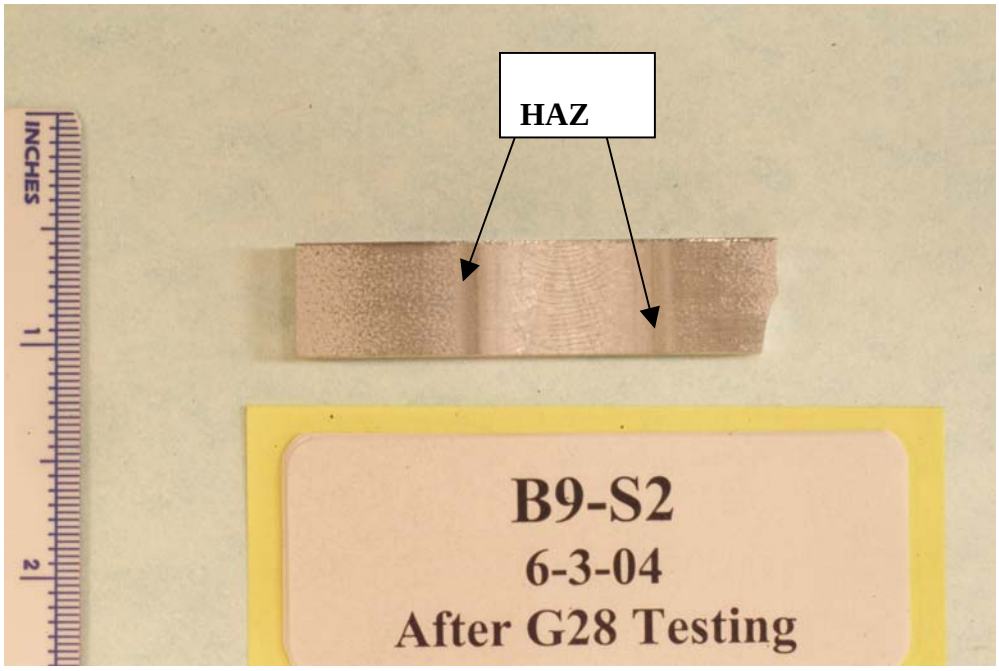

Figure 2.2b

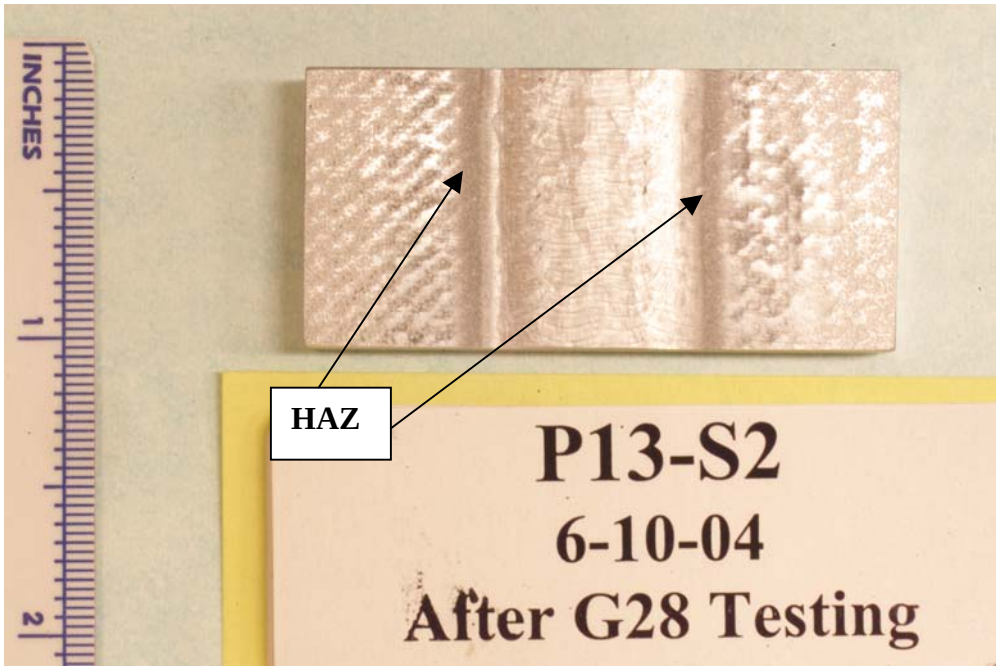

Figure 2.2c

Figure 2.2 - Appearance of the coupons after the tests. The dark lines at both sides of the weld show intergranular attack in the heat-affected zone. The identification of the coupons is given in Table 2.2

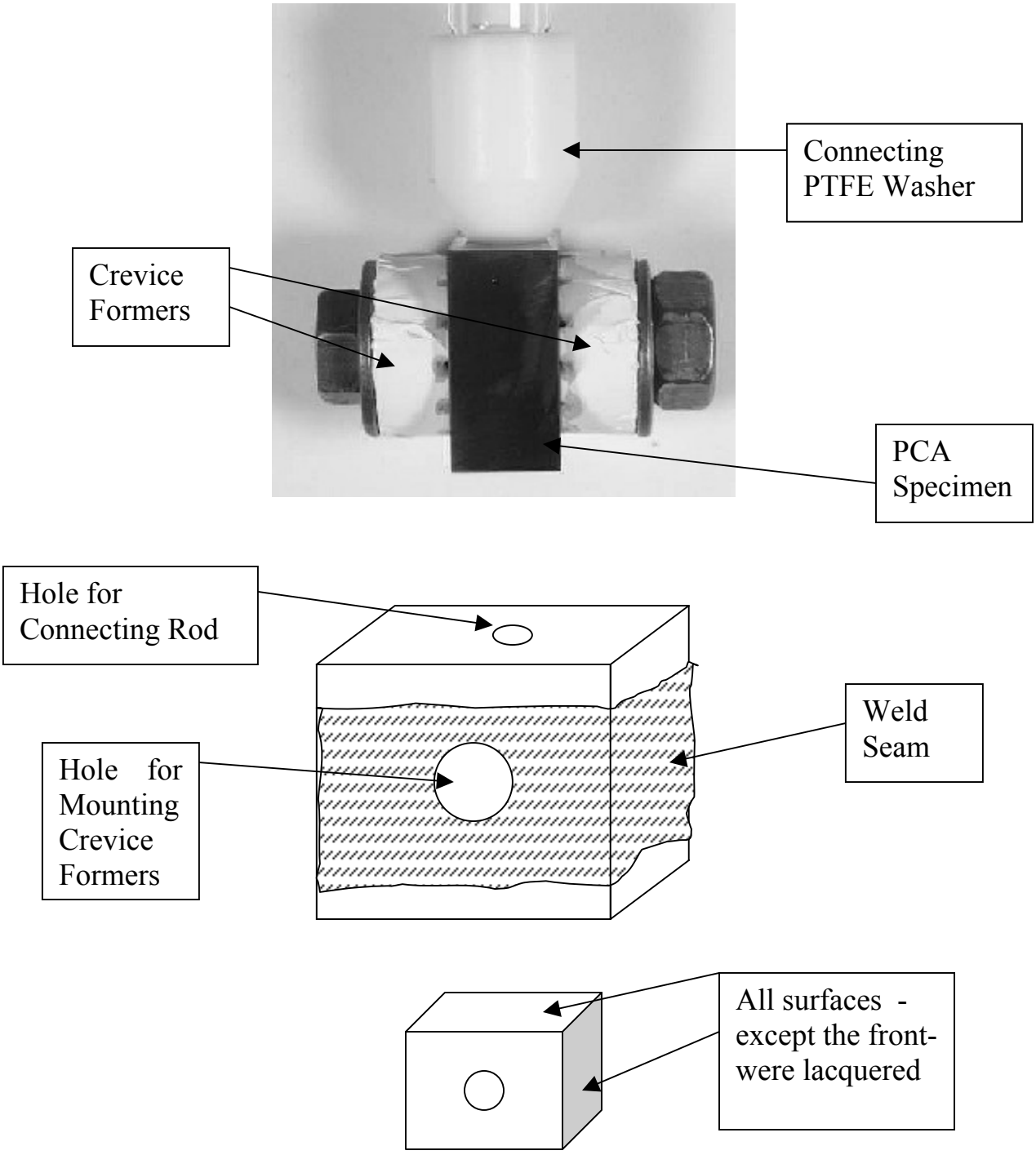

Figure 2.3 - PCA Specimen (0.75 x 0.75 x 0.375 inch or approx. 20 x 20 x 10 mm). The exposed surface area for testing was 3.27 cm².

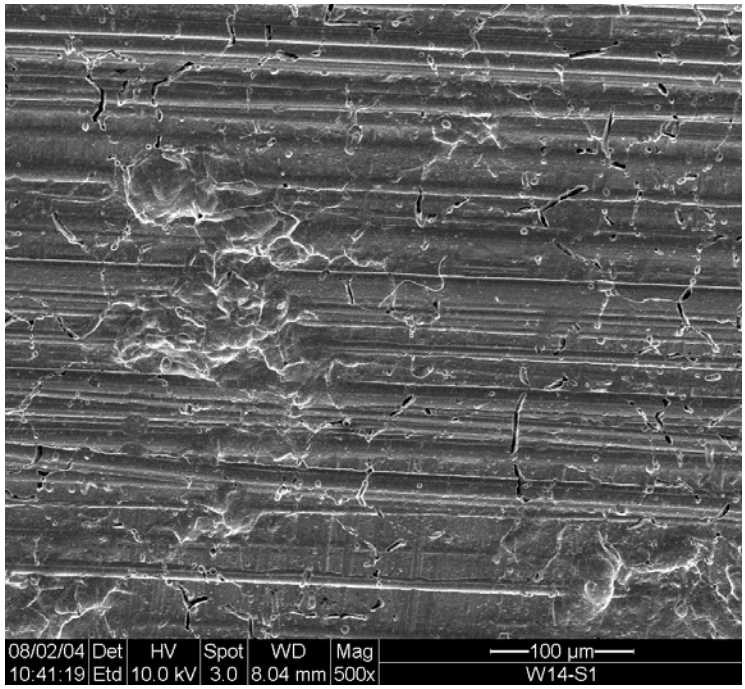

Figure 2.4 - SEM Image of ASW Coupon W14-S1 showing IGA in the base metal away from the weld seam. Magnification X 500

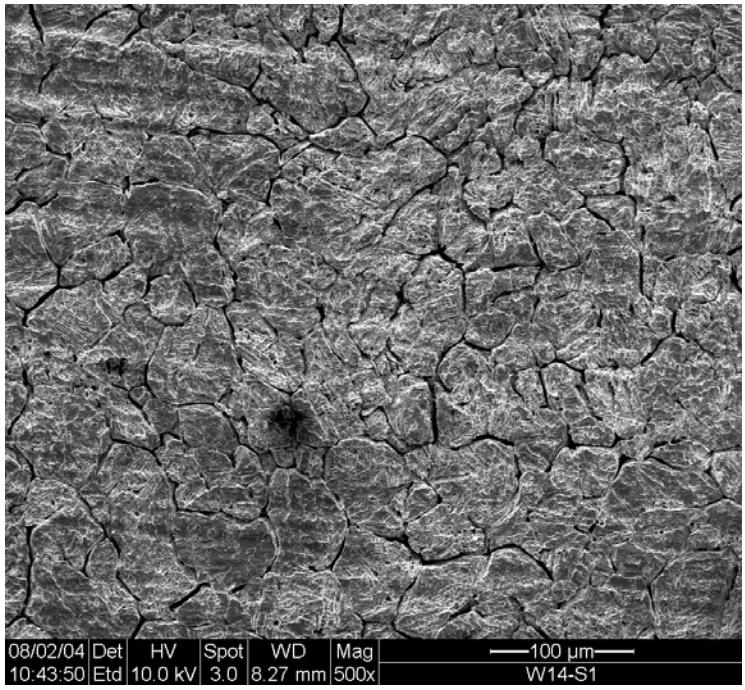

Figure 2.5 - SEM Image of ASW Coupon W14-S1 showing IGA in the base metal in the HAZ area. Magnification X 500

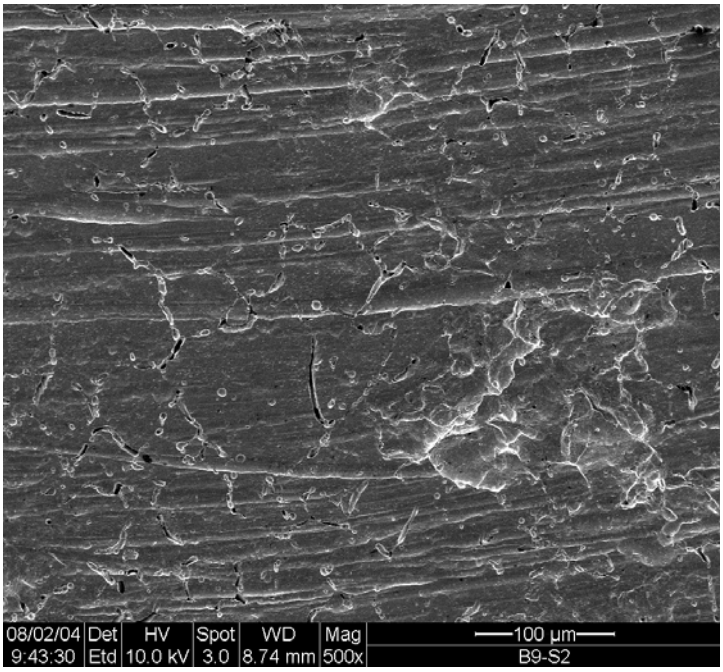

Figure 2.6 - SEM Image of LPB Coupon B9-S2 showing IGA in the base metal away from the weld seam. Magnification X 500

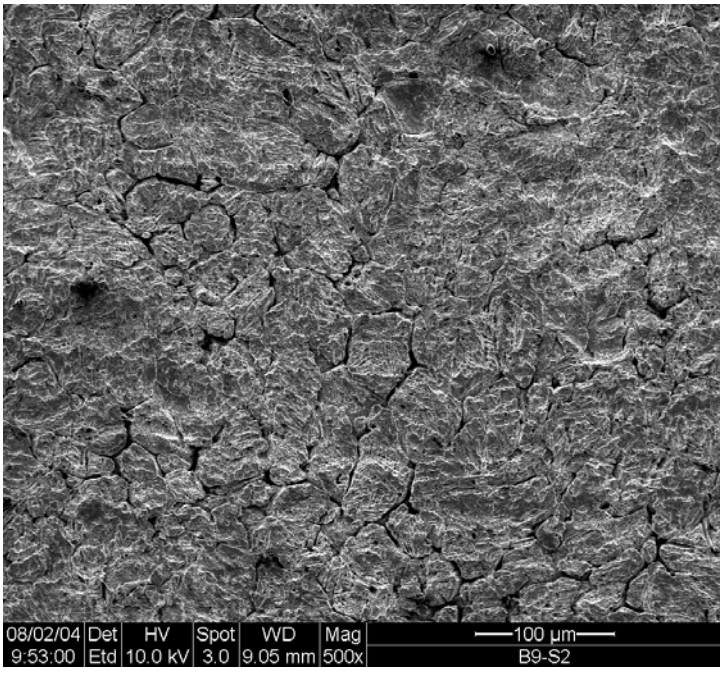

Figure 2.7 - SEM Image of LPB Coupon B9-S2 showing IGA in the base metal in the HAZ area. Magnification X 500

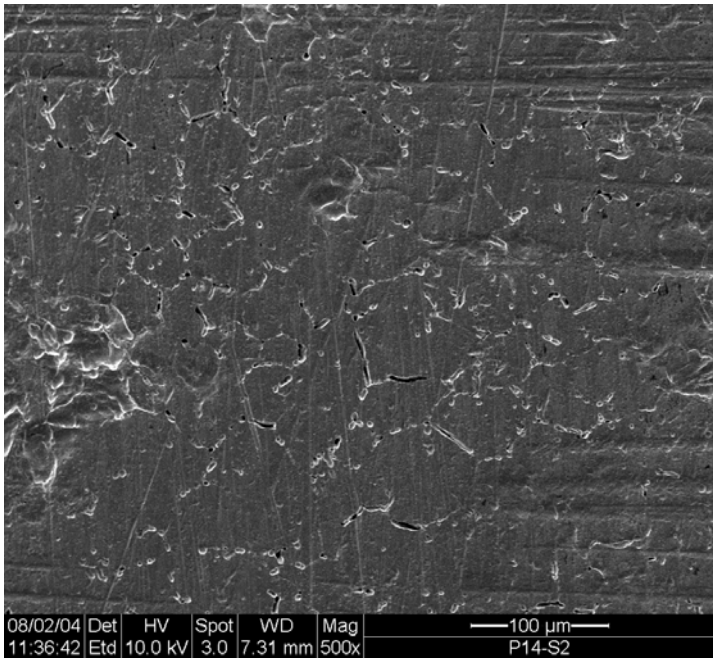

Figure 2.8 – SEM image of the LSP Coupon P14-S2 showing IGA in the base metal away from the weld seam. Magnification X 500

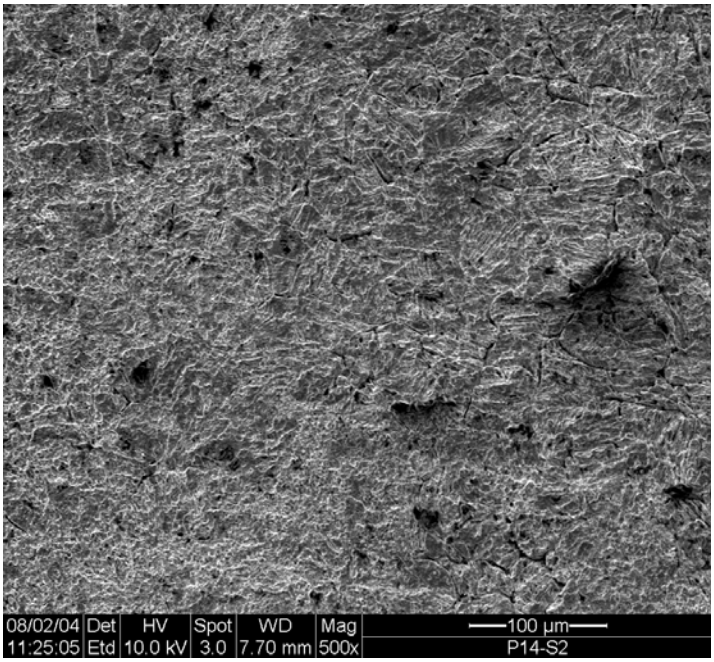

Figure 2.9 - SEM Image of LSP Coupon P14-S2 showing IGA in the base metal in the HAZ area. Magnification X 500

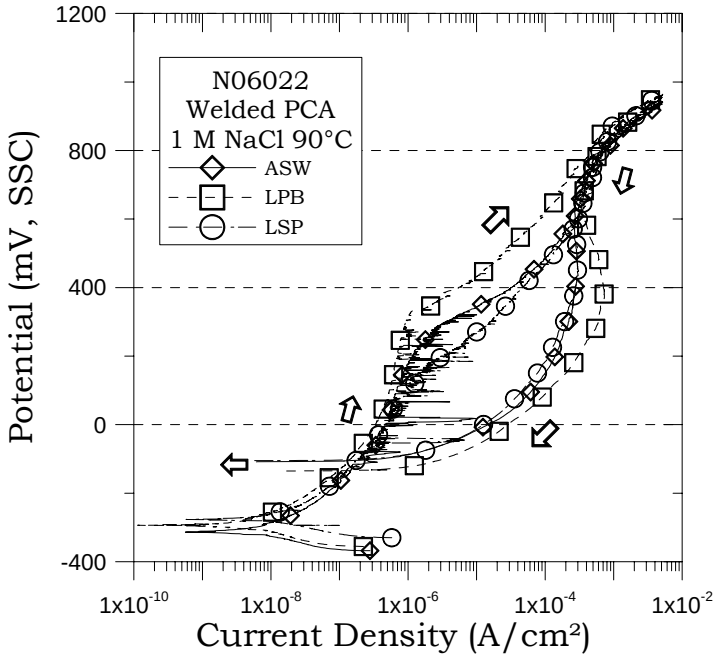

Figure 2.10 - CPP of Alloy 22 in 1 M NaCl at 90°C.
Similar behavior found for ASW, LPB and LSP materials

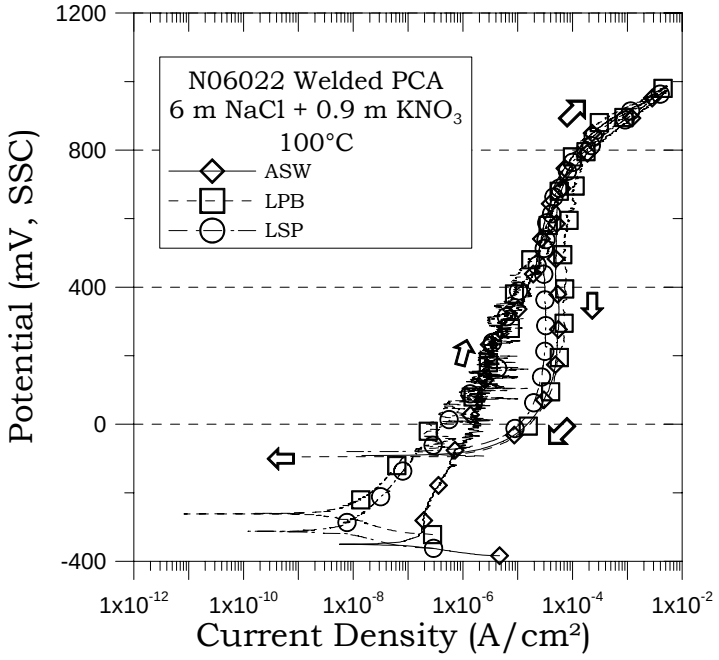

Figure 2.11 - CPP of Alloy 22 in 1 M NaCl at 90°C.
Similar behavior found for ASW, LPB and LSP materials

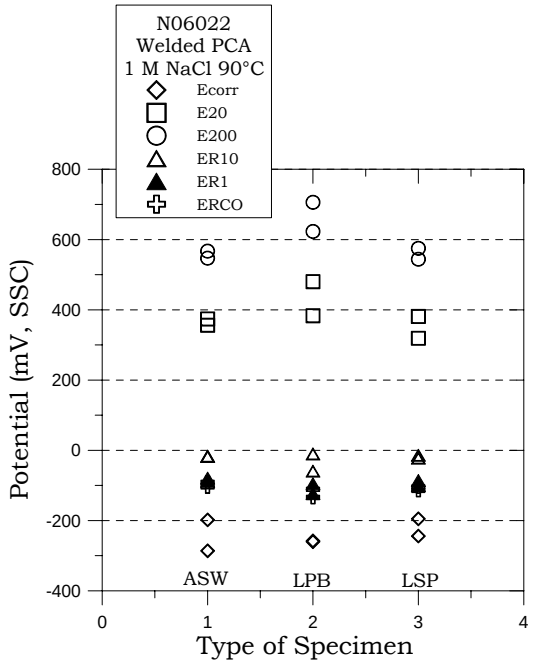

Figure 2.12 - Characteristic Potentials from CPP Curves for the three N06022 Materials in 1 M NaCl at 90°C.

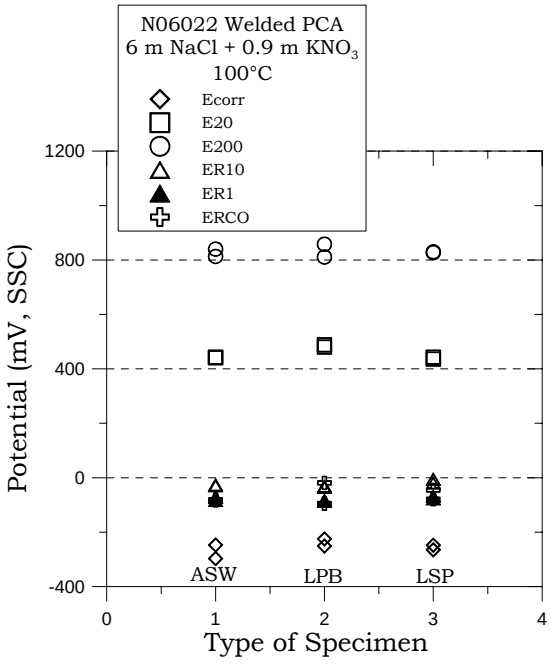

Figure 2.13 - Characteristic Potentials from CPP Curves for the three N06022 Materials in 6 m NaCl + 0.9 m KNO_3 at 100°C

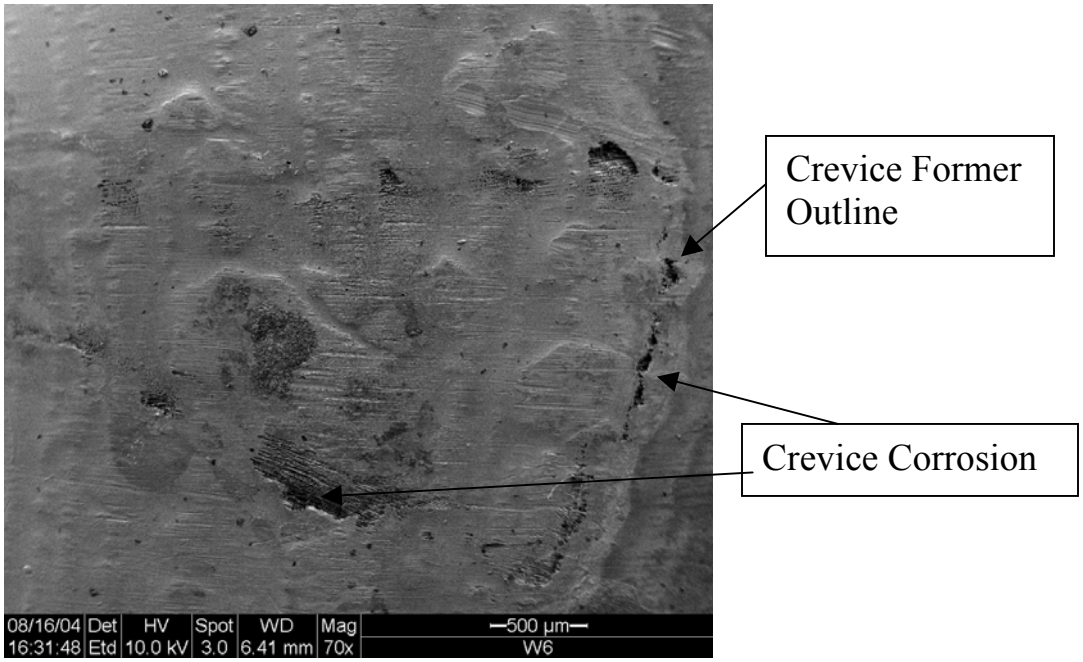

Figure 2.14 - SEM image of ASW Specimen W6 Tested in 1 M NaCl at 90°C The surface does not appear flat. Magnification X 70

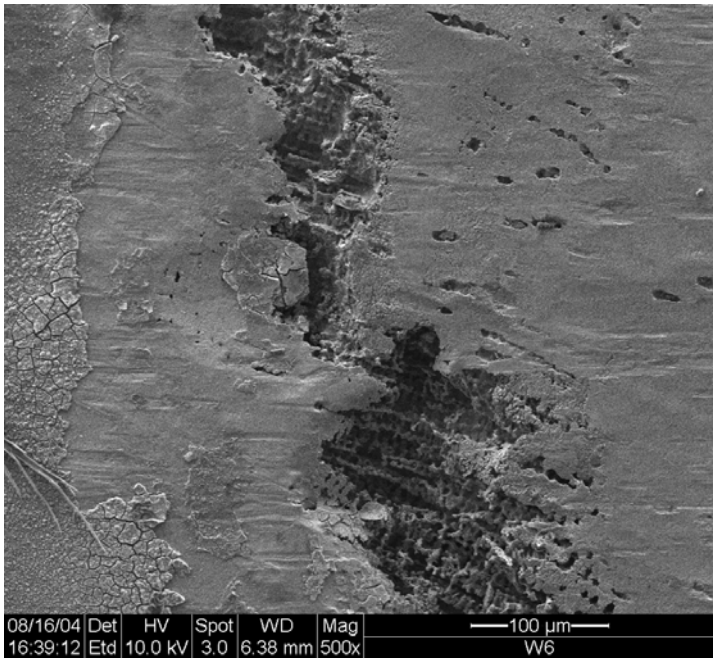

Figure 2.15 - SEM image of ASW Specimen W6 Tested in 1 M NaCl at 90°C. Crevice Attack is Interdendritic. Magnification X 500

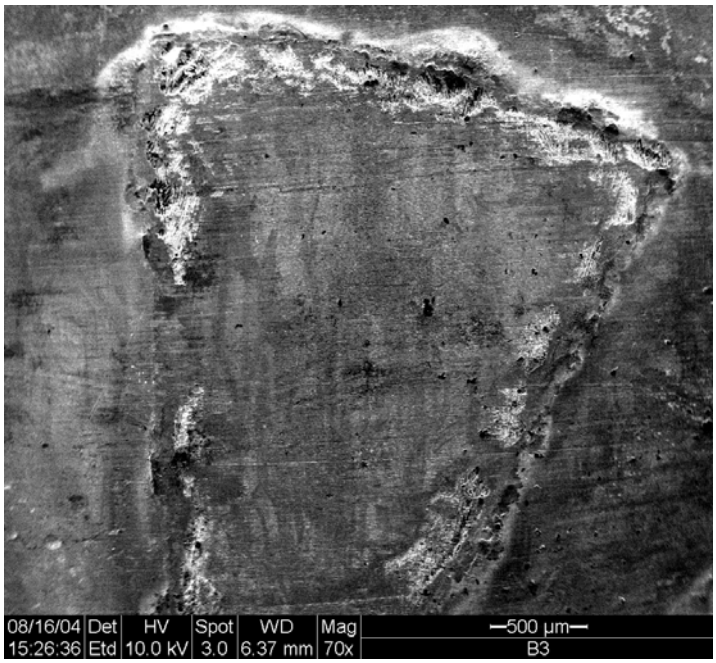

Figure 2.16 - SEM image of LPB Specimen B3 Tested in 1 M NaCl at 90°C. The surface does not appear flat. Magnification X 70

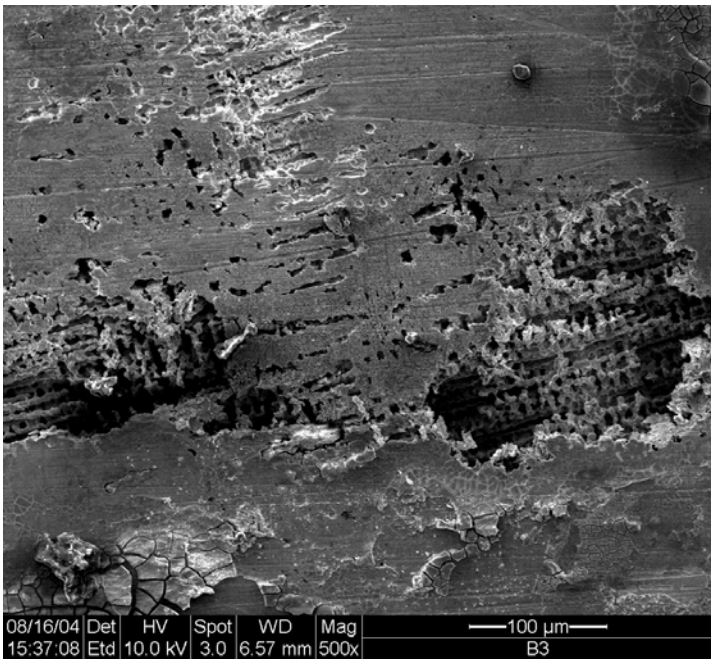

Figure 2.17 - SEM image of LPB Specimen B3 Tested in 1 M NaCl at 90°C. Crevice Attack is interdendritic. Magnification X 500

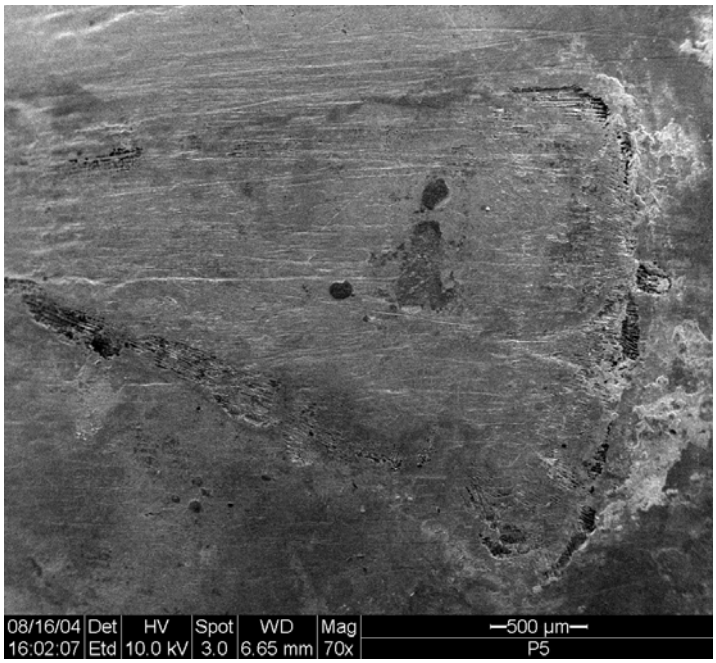

Figure 2.18 - SEM image of LSP Specimen P5 Tested in 1 M NaCl at 90°C The surface does not appear flat. Magnification X 70

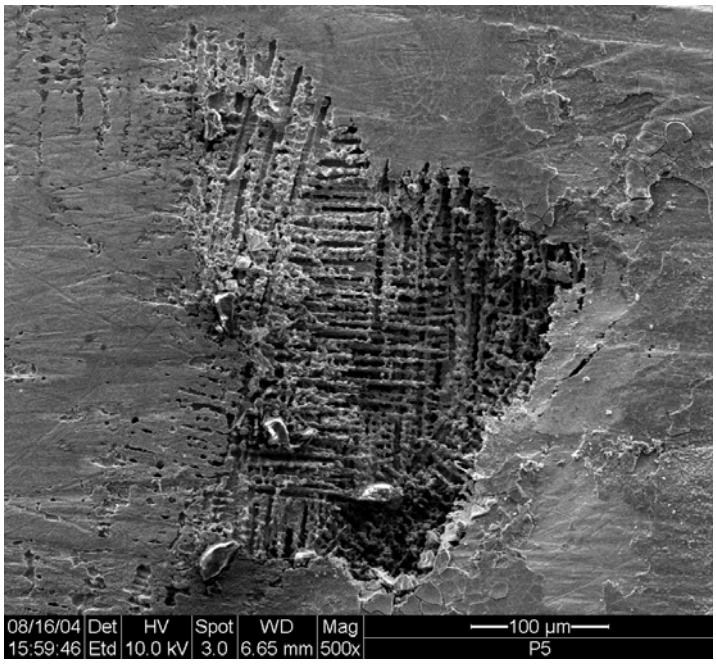

Figure 2.19 - SEM image of LSP Specimen P5 Tested in 1 M NaCl at 90°C. Crevice Attack is interdendritic. Magnification X 500

3. Testing of Specimens from a Mockup Container

3.1. Introduction

The impact of fabrication processes such as rolling and thick section welding during the manufacturing of a full diameter mockup container was studied under the FY04 technical work plan (TWP) AWPT47. Testing was directed by John C. Estill and Tammy Summers. The electrochemical tests were carried out by Kenneth J. King. The experimental details of this work are documented in SN-LLNL-SCI-452-V3, pages 85-100. The data is in TDMS under DTN LL050302312251.129.

Alloy 22 (N06022) was selected by expert elicitation as the material for the corrosion resistant outer barrier. [1] Alloy 22 belongs to the family of the Nickel (Ni)-Chromium (Cr)-Molybdenum (Mo) corrosion resistant alloys. [2-3] Alloy 22 has been extensively characterized in the laboratory for its resistance to general or passive corrosion, localized corrosion and stress corrosion cracking. [1] A full-diameter, quarter-length mockup of the Alloy 22 was package has been fabricated for testing (Figure 21 in Reference 1). [1] The welding and other fabrication parameters are in MOL20040525.0174.

It was important to test the corrosion resistance of specimens prepared from the full-diameter fabricated container to determine if industrial processes such as cold rolling, welding and annealing may affect the corrosion behavior of Alloy 22. Electrochemical testing was carried out in a variety of environments for which YMP had data from previous testing using standard prepared specimens from flat plates.

Keywords: N06022, Container Fabrication, Mockup, Welding, Corrosion Rate, Repassivation Potential

3.2. Experimental

3.2.1. Preparation of the Specimens

Alloy 22 (N06022) specimens for the tests were machined from 2-inch diameter hockey-puck shaped samples, which were machined from the full-diameter container prototype (MOL20040525.0174). The hockey pucks were removed from the longitudinal weld of the mockup container. The heat number of the base plate used for fabrication was 058371LE2 and the heat number for the weld wire was XX1829BG. The weld seam in the hockey pucks was approximately 1-3/16” wide. The hockey pucks samples used to fabricate the anodic behavior specimens were designated: L2, L3, L4, L5, L6 and L7 by the provider of these samples. That is, from six hockey pucks twelve electrochemical specimens were fabricated. The prism crevice assembly (PCA) specimens were fabricated at LTI (Hatfield, PA) and labeled from AY001 to AY012. The tested surface area of the PCA specimens was 14.06 cm². The crevicing mechanism for these PCA tests was based on ASTM G 48 12-tooth washer. [4-6] To provide a tight crevice, the washer was made of a ceramic material and it was covered by PTFE tape. The PCA specimens were degreased in acetone and DI water, let dry in air before testing.

3.2.2. Electrolyte Solution and Testing Procedure

Electrochemical tests were carried in deaerated simple salt solutions listed in Table 3.1. The electrolyte solutions were selected based on previous experience in the project where crevice repassivation potentials were available. These solutions represent aggressive hot environments of pure chloride conditions (NaCl or $CaCl_2$) and chloride plus nitrate environments. Nitrate is an inhibitor for crevice corrosion in Alloy 22. Nitrogen (N_2) was purged through the solution at a flow rate of 100 cc/min for 24 hours while the corrosion potential (E_{corr}) was monitored. Nitrogen bubbling was carried throughout all the electrochemical tests. The electrochemical tests were conducted in a one-liter, three-electrode, borosilicate glass flask (ASTM G 5). [7] A water-cooled condenser combined with a water trap was used to maintain solution concentration and avoid the ingress of air. The temperature of the solution was controlled using a heating mantle and a thermocouple immersed in the solution. All the tests were carried at ambient pressure. The reference electrode was saturated silver chloride (SSC) electrode, which has a potential of 199 mV more positive than the standard hydrogen electrode (SHE). The reference electrode was connected to the solution through a water-jacketed Luggin probe so that the electrode was maintained at near ambient temperature. The counter electrode was a flag (36 cm^2) of platinum foil spot-welded to a platinum wire. All the potentials in this paper are reported in the SSC scale.

Basically the test sequence for each specimen consisted of three parts: (1) E_{corr} evolution as a function of time for 24 h, (2) Polarization Resistance (ASTM G 59) three subsequent times and (3) A larger anodic polarization to determine susceptibility to crevice corrosion. The larger anodic polarization was conducted using Cyclic Potentiodynamic Polarization (CPP) method (ASTM G 61). [7]

Polarization Resistance (ASTM G 59) - Corrosion rates (CR) were obtained using the polarization resistance method (ASTM G 59). [7] Each one of these tests lasts approximately four minutes. An initial potential of 20 mV below the corrosion potential (E_{corr}) was ramped to a final potential of 20 mV above E_{corr} at a rate of 0.167 mV/s. Linear fits were constrained to the potential range of 10 mV below E_{corr} to 10 mV above E_{corr}. During the fitting of the data to calculate the polarization resistance (Rp), the potential (E) was plotted in the X-axis. The Tafel constants, b_a and b_c, were assumed to be + 0.12 V/decade. Corrosion rates were calculated using Equation 3.1

$$i_{corr} = \frac{1}{R_p} \times \frac{b_a \cdot b_c}{2.303(b_a + b_c)}$$

$$CR(\mu m / yr) = k \frac{i_{corr}}{d} EW \qquad (3.1)$$

Where k is a conversion factor (3.27 x 10^9 $nm \cdot g \cdot A^{-1} \cdot cm^{-1} \cdot yr^{-1}$), i_{corr} is the corrosion current density in A/cm^2 (calculated from the measurements of the resistance to polarization, R_p), EW is the equivalent weight, and d is the density of Alloy 22 (8.69 g/cm^3). Assuming an equivalent

dissolution of the major alloying elements as Ni^{2+}, Cr^{3+}, Mo^{6+}, Fe^{2+}, and W^{6+}, the EW for Alloy 22 is 23.28 (ASTM G 102). [7]

Cyclic Potentiodynamic Polarization - CPP (ASTM G 61) - The test to assess the susceptibility of Alloy 22 to localized corrosion and passive stability was the cyclic potentiodynamic polarization technique, CPP (ASTM G 61). [7] The potential scan was started 100 mV below Ecorr at a set scan rate of 0.167 mV/s. The scan direction was reversed when the current density reached 5 mA/cm^2 in the forward scan. Depending on the range of applied potentials, each CPP test could last between 1 h and 3 h. From the polarization curve, several parameters of importance can be extracted. The E20 and E200 represent values of breakdown potential and ER10, ER1 and ERCO represent values of repassivation potential in the reverse scan of the CPP. ERCO is the potential at which the reverse scan intersects the forward scan. [4,5] Table 3.2 lists these potential parameters for all the tested specimens.

3.3. Results from Electrochemical Testing

3.3.1. The Corrosion Potential (24-h)

Table 3.2 shows the average 24-h E_{corr} of the Alloy 22 specimens prepared using hockey pucks removed from the mockup container for six different deaerated electrolyte solutions. The values in Table 3.2 are short term E_{corr} in deaerated solutions and may not represent the steady-state E_{corr} for the alloy exposed to the same electrolytes for long time in aerated conditions. The 24-h E_{corr} values in each electrolyte and temperature were surprisingly reproducible, except for the 6 m NaCl + 0.9 m KNO_3 ($[Cl^-]/[NO_3^-]$= 6.67) at 80°C. The lowest E_{corr} corresponded to the 1 M NaCl at 90°C and the highest E_{corr} corresponded to the most concentrated solution, which is also the solution with the highest concentration of nitrate (12 m $CaCl_2$ + 6 m $Ca(NO_3)_2$ $[Cl^-]/[NO_3^-]$= 6.67 at 130°C). The E_{corr} in the 6 m NaCl + 0.9 m KNO_3 solution with a ratio $[Cl^-]/[NO_3^-]$ = 6.67) seemed to –as expected- decrease when the temperature increased from 80°C to 100°C.

3.3.2. The Corrosion Rate (After 24-h Immersion

Table 3.2 shows the average corrosion rates for the Alloy 22 specimens prepared from the hockey pucks that were removed from the mockup container. These corrosion rates were obtained after 24 h exposure in deaerated electrolytes. It is expected that these corrosion rates will decrease for longer immersion times, especially under aerated conditions. [8] In spite of the short exposure time, the corrosion rates in Table 3.2 were low (less than 1 μm/year). The highest measured corrosion rate corresponded to the 1 M NaCl solution at 90°C (which had the lowest or more active E_{corr}) and the lowest corrosion rate was for the 12 m $CaCl_2$ + 6 m $Ca(NO_3)_2$ solution even though this electrolyte had the highest temperature (130°C) (but appropriately had also the highest E_{corr}). The corrosion rate for the Alloy 22 specimens in the other four solutions (Table 2) were similar to each other and between 0.2 and 0.4 μm/year.

3.3.3. Cyclic Potentiodynamic Polarization (CPP) and The Repassivation Potential

Table 3.2 shows parameters obtained from the cyclic potentiodynamic polarization (CPP) curves from the 12 tested specimens. These parameters can be divided between breakdown potentials (E20 and E200) in the forward scan of CPP and repassivation potentials (ER10, ER1 and ERCO) from the reverse scan. The higher the breakdown potential the higher the potential that needs to be applied to the alloy to force it to corrode rapidly. Table 3.2 shows that the highest breakdown potential corresponded to the high nitrate solution 12 m $CaCl_2$ + 6 m $Ca(NO_3)_2$ $[Cl^-]/[NO_3^-]$ = 6.67 at 130°C, confirming the inhibition effect by nitrate in spite of the highest temperature of this electrolyte. The lowest breakdown potentials corresponded to the 5 M $CaCl_2$ solution at 90°C, showing that the passivity of Alloy 22 was most unstable in this concentrated pure chloride solution.

Once the breakdown occurs, the repassivation potential indicates the potential that needs to be applied for the alloy to regain a passive behavior similar to that before breakdown. The lowest repassivation potential was for the 5 M $CaCl_2$ solution at 90°C, again suggesting that in this solution it is more difficult to repassivate Alloy 22 once the breakdown occurs. In the solution 6 m NaCl + 0.9 m KNO_3 at 100°C, the breakdown potentials were rather positive but the repassivation potentials were low, that is, the chromium oxide film was initially resistant to breakdown but once localized corrosion was nucleated, the repassivation potentials were rather low (similar to that of 1 M NaCl at 90°C). The solutions at the lower temperature (80°C) and the solution with high nitrate 12 m $CaCl_2$ + 6 m $Ca(NO_3)_2$ had the highest repassivation potentials, even though the latter solution was at a higher temperature (130°C).

3.3.4. Corrosion Mode

Table 3.1 describes the corrosion characteristics of all the tested specimens after the cyclic potentiodynamic polarization (CPP) tests through optical observation in a stereomicroscope at X20 magnification. Figure 3.1 shows one of the corroded specimens after the CPP in 5 M $CaCl_2$ at 90°C. Figure 3.1 shows a typical mode of attack of Alloy 22 in this solution. This mode of corrosion has been observed and described before. [4-5] The attack in Figure 3.1 is termed massive localized corrosion. It is a localized corrosion since it starts at one spot (generally at the crevice former or gasket interface with the metal). It then propagates over the rest of the specimen following the direction of gravity. Figure 3.2 shows that the massive attack can also start as corrosion pits on the non-creviced surface of the specimen (short-transverse section of the PCA specimen) and propagating down producing a reverse comet-like feature.

Figures 3.3 and 3.4 show the specimens polarized in 12 m $CaCl_2$ + 6 m $Ca(NO_3)_2$ at 130°C. Even though the temperature was 40°C higher and the specimens were polarized to 900 mV higher than for the specimens tested in 5 M $CaCl_2$ at 90°C (Figures 3.1 and 3.2), the attack shown in Figures 3.3 and 3.4 was more contained than in Figures 3.1 and 3.2. This could be related to the beneficial effect of nitrate in the solution. In the $CaCl_2$ + $Ca(NO_3)_2$ solution the attack occurred only on the metal surface exposed to the bold solution, away from the crevice formers (Figures 3.3 and 3.4). The attack in Figures 3.3-3.4 could be associated with a form of pitting corrosion, even though the attack in Alloy 22 is shallow and wide as compared to the typical pitting corrosion observed for example in austenitic stainless steels. [9] Figure 3.5 shows

the corrosion mode of Alloy 22 after CPP test in 1 M NaCl at 90°C. The appearance of the specimen is typical for this type of environment. [1-2] There is a yellow and iridescent transpassivity in the boldly exposed surfaces and deep crevice corrosion following the outline of the crevice formers in the occluded areas. [4-5] The crevice corrosion attack is bright and crystallographic, showing outlines of grains and even planes inside of the grains.

Figures 3.6 and 3.7 show the effect of the temperature on the Alloy 22 susceptibility to crevice corrosion in 6 m NaCl + 0.9 m KNO_3. At 80°C, the specimen shows mostly iridescent transpassivity in the boldly exposed surfaces and little or no dull crevice corrosion under the crevice formers (Figure 3.6). At 100°C (Figure 3.7), the specimen shows a higher amount of dull crevice corrosion and also some spots of crystalline crevice corrosion. The aspect of the crystallographic crevice corrosion is similar to types of attack found in pure chloride solution (for example in 1 M NaCl, Figure 3.5).

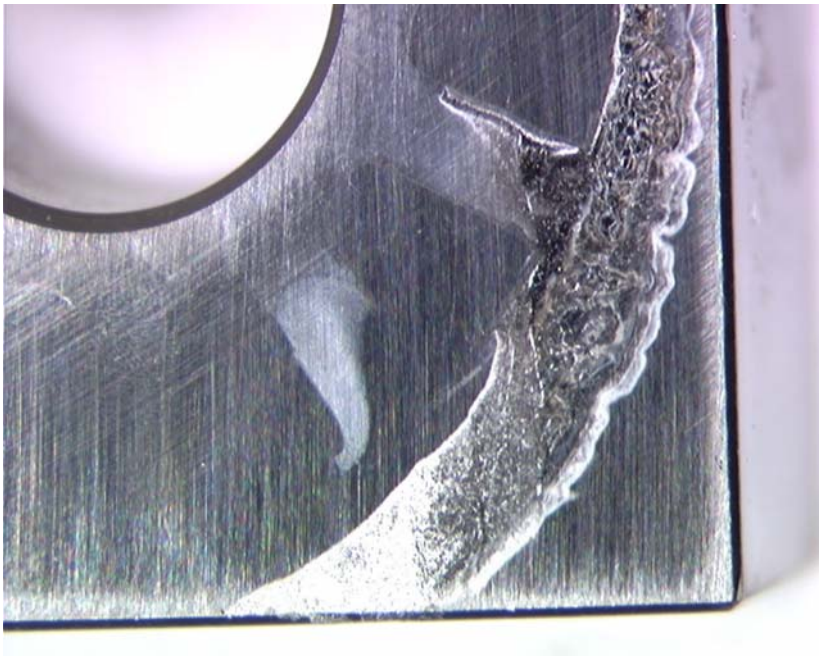

Figure 3.1 - Alloy 22 Specimen AY008 after CPP testing in 5 M $CaCl_2$ at 90°C showing Typical Massive Localized Attack, Magnification ~X 8

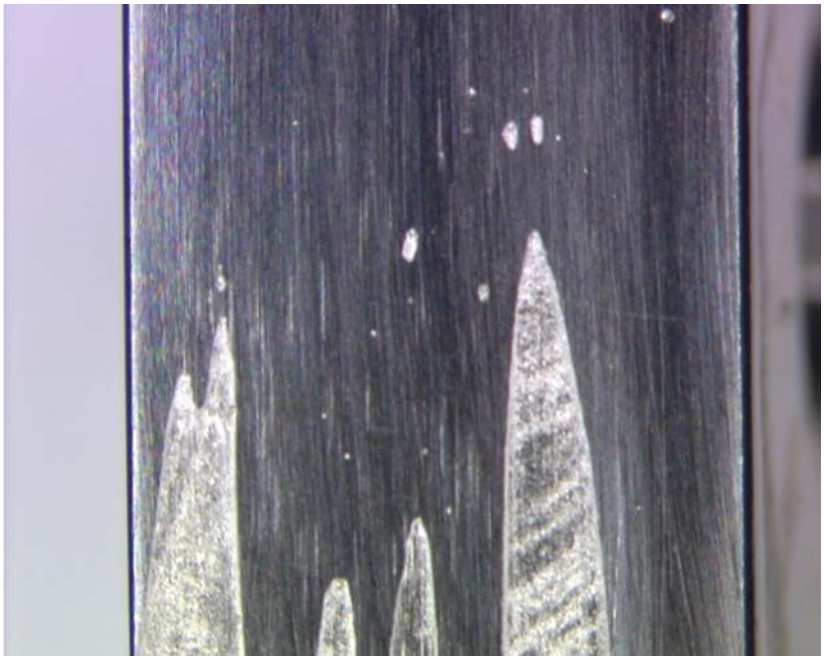

Figure 3.2 - Alloy 22 Specimen AY008 after CPP testing in 5 M $CaCl_2$ at 90°C showing Typical Massive Localized Attack on the ST, Non-Creviced Face

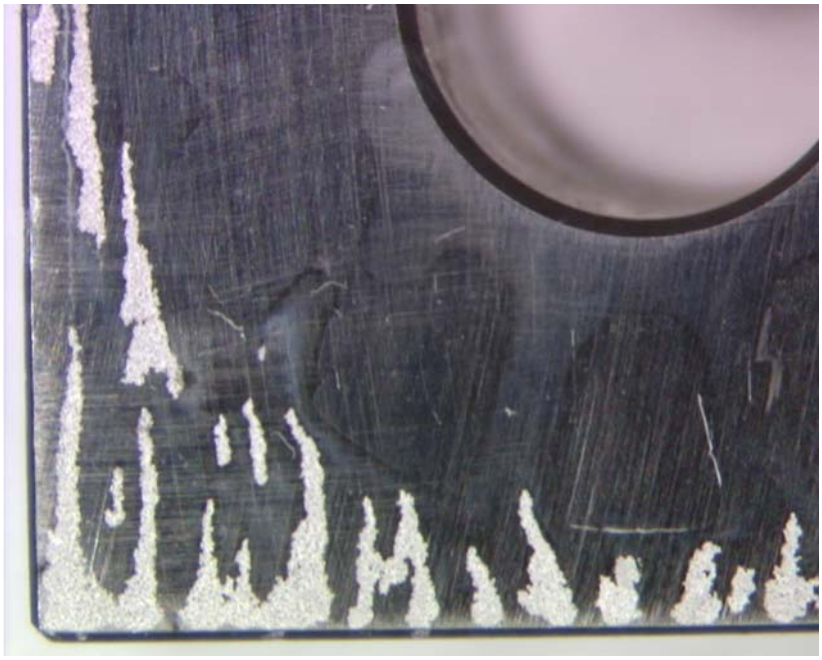

Figure 3.3 - Alloy 22 Specimen AY011 after CPP in 12 m $CaCl_2$ + 6 m $Ca(NO_3)_2$ at 130°C Magnification ~X 8

Figure 3.4 - Alloy 22 Specimen AY011 after CPP in 12 m $CaCl_2$ + 6 m $Ca(NO_3)_2$ at 130°C showing Localized Attack on the ST Face (non-creviced), Magnification ~X 8

Figure 3.5 - Alloy 22 Specimen AY009 after CPP in 1 M NaCl at 90°C showing Major Transpassivity in the bold areas. Crevice Corrosion under CF, Magnification ~X 8

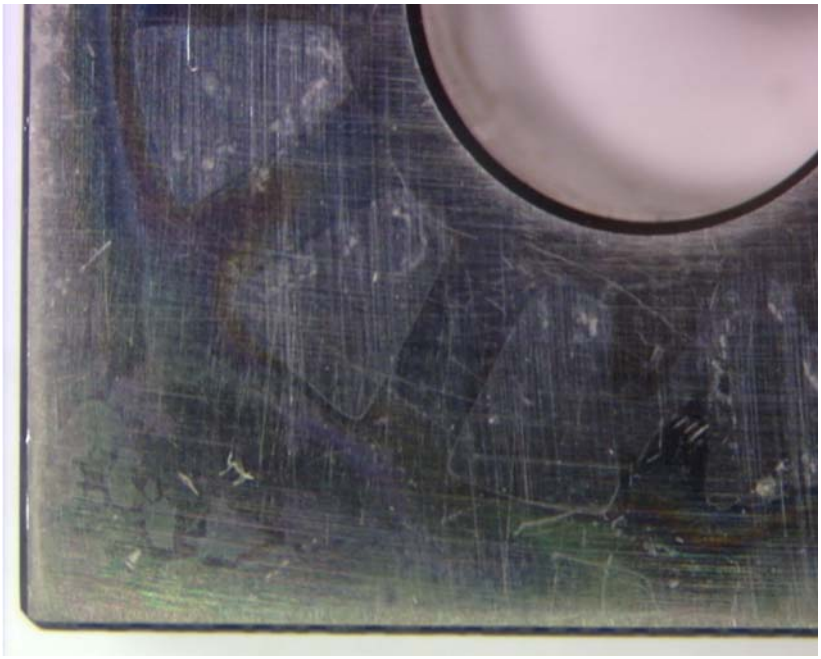

Figure 3.6 - Alloy 22 Specimen AY003 after CPP in 6 m NaCl + 0.9 m KNO_3 at 80°C showing Transpassivity in the bold areas and Little or no Dull Crevice Corrosion under CF, Magnification ~X 8

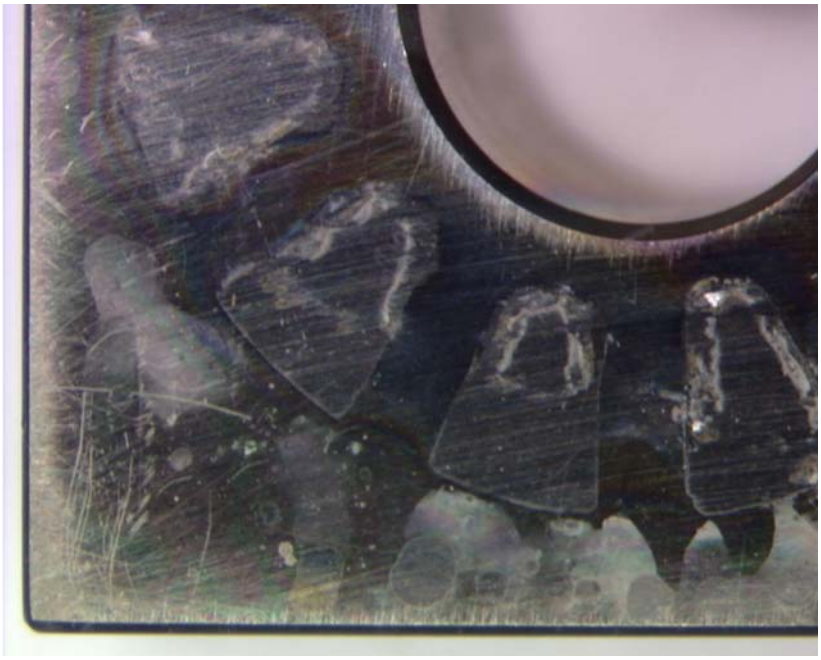

Figure 3.7 - Alloy 22 Specimen AY003 after CPP in 6 m NaCl + 0.9 m KNO_3 at 100°C showing Transpassivity in the bold areas and Mostly Dull Crevice Corrosion under CF, Magnification ~X 8

3.3.5. Comparison with Archive Data

Table 3.3 shows comparative data between the values of repassivation potential obtained as part of this work (Table 3.2) and the available data on other type of Alloy 22 specimens in the same environments (salt composition and temperature). Table 3.3 shows that the results currently presented and the known values of repassivation potential for Alloy 22 are the same. The corollary is that under the tested conditions, the material removed from the mockup behaved the same as the material from laboratory prepared flat plates. In other words, the values of repassivation potential used to prepare the localized corrosion degradation model for the waste package [10] would also accurately represent the behavior of material from a fabricated container.

3.4. Conclusions

(1) Under the tested conditions, the repassivation potentials (ER1 and ERCO) obtained using specimens prepared from a prototype container had similar values as the repassivation potentials currently available for specimens fabricated using laboratory welded flat plates

(2) Values of repassivation potential used in the models to predict the lifetime of the container via localized corrosion accurately represent the behavior of a fabricated container.

3.5. References

1. G. M. Gordon, Corrosion, 58, 811 (2002)
2. R. B. Rebak and P. Crook, "Influence of the Environment on the General Corrosion Rate of Alloy 22," PVP-ASME Vol. 483, pp. 131-136 (American Society of Mechanical Engineers, 2004: New York, NY).
3. ASTM International, Volume 02.04 "Non-Ferrous Metals" Standard B 575 (ASTM International, 2002: West Conshohocken, PA)
4. K. J. Evans, L. L. Wong and R. B. Rebak "Determination of the Crevice Repassivation Potential of Alloy 22 by a Potentiodynamic-Galvanostatic-Potentiostatic Method," PVP-ASME Vol. 483, pp. 137-149 (American Society of Mechanical Engineers, 2004: New York, NY).
5. K. J. Evans, A. Yilmaz, S. D. Day, L. L. Wong, J. C. Estill and R. B. Rebak "Comparison of Electrochemical Methods to Determine Crevice Corrosion Repassivation Potential of Alloy 22 in Chloride Solutions," JOM, p. 56, January 2005

6. G. O. Ilevbare, K. J. King, S. R. Gordon, H. A. Elayat, G. E. Gdowski and T. S. E. Summers “Effect of Nitrate on the Repassivation Potential of Alloy 22 in Chloride Containing Solutions,” Fall 2004 Meeting of the Electrochemical Society, 03-08Oct04, Honolulu, HI (to be published).

7. ASTM International, Volume 03.02, Standards G 5, G 15, G 48, G 59, G 61, G 102 (ASTM International, 2003: West Conshohocken, PA).

8. K. J. King, J. C. Estill, G. A. Hust, M. L. Stuart and R. B. Rebak “Evolution of the Corrosion Potential and Corrosion Rate for Alloy 22 in Chloride plus Nitrate Brines,” CORROSION/2005, Paper 05607 (NACE International, 2005: Houston, TX)

9. A. J. Sedricks “Corrosion of Stainless Steels” (John Wiley & Sons, Inc., 1996: New York, NY)

10. J. H. Lee, T. Summers and R. B. Rebak, Paper 04692, Corrosion/2004 (NACE International, 2004: Houston, TX)

Table 3.1 -
Specimens, Testing Conditions and Observed Results after CPP

Specimens	Solutions	T (°C)	Observations
AY001	6 m NaCl + 0.3 m KNO_3	80	Transpassivity, yellow iridescent, little dull CC
AY002	6 m NaCl + 0.3 m KNO_3	80	
AY003	6 m NaCl + 0.9 m KNO_3	80	Transpassivity, yellow iridescent, little dull CC
AY004	6 m NaCl + 0.9 m KNO_3	80	
AY005	6 m NaCl + 0.9 m KNO_3	100	Transpassivity and –mostly dull- CC
AY006	6 m NaCl + 0.9 m KNO_3	100	
AY007	5 M $CaCl_2$	90	Massive attack outside CF, IGA on base metal, PC on ST face
AY008	5 M $CaCl_2$	90	
AY009	1 M NaCl	90	Transpassivity, yellow, abundant deep CC
AY010	1 M NaCl	90	
AY011	11.4 m $CaCl_2$ + 5.4 m $Ca(NO_3)_2$	130	Substantial string-like localized attack outside CF
AY012	11.4 m $CaCl_2$ + 5.4 m $Ca(NO_3)_2$	130	
CC= Crevice Corrosion, CF = Crevice Former, IGA = Intergranular Attack, PC = Pitting Corrosion, ST = Short Transverse			

Table 3.2 -

Short Term Deaerated Corrosion Potential and Corrosion Rate and Parameters from CPP. All Potentials in mV, SSC

Specimens	E_{corr} 24 h	CR (µm/year)	E20	E200	ER10	ER1	ERCO
AY001	153	0.239, 0.225, 0.192	787	859	761	686	714
AY002	-43	0.430, 0.465, 0.528	786	843	743	430	682
Average	55	0.347	787	851	752	558	698
SD	139	0.144	1	11	13	181	23
AY003	-452	0.362, 0.302, 0.292	738	846	700	582	NA
AY004	-433	0.178, 0.149, 0.147	701	848	684	535	NA
Average	-443	0.238	720	847	692	559	
SD	13	0.092	26	1	11	33	
AY005	-473	0.334, 0.279, 0.324	465	776	554	-52	-75
AY006	-453	0.218, 0.209, 0.226	588	787	597	-34	-74
Average	-463	0.265	527	782	576	-43	-75
SD	14	0.055	87	8	30	13	1
AY007	-384	0.963, 0.870, 0.815	108	138	-52	-93	-73
AY008	-352	0.361, 0.370, 0.300	112	139	-78	-154	-169
Average	-368	0.613	110	139	-65	-124	-121
SD	23	0.3	3	1	18	43	68
AY009	-523	1.917, 1.705, 1.590	441	713	69	-42	-54
AY010	-535	1.718, 1.562, 1.398	486	724	78	-44	-52
Average	-529	1.648	464	719	74	-43	-53
SD	8	0.175	32	8	6	1	1
AY011	108	0.092, 0.096, 0.091	931	1038	798	760	783
AY012	41	0.192, 0.184, 0.181	762	1027	801	781	811
Average	75	0.139	847	1033	800	771	797
SD	47	0.051	120	8	2	15	20

Table 3.3 -

Comparison Between Current (Table 2) and Archive Results or Repassivation Potentials. All Potentials in mV, SSC

Material/ Data Source	**ER1**	**ERCO**	**ER, CREV**
1 M NaCl, 90°C			
Current PCA Mockup (Table 2)	-43 ± 1	-53 ± 1	NA
Archive MA MCA Ref. 4-5	-80 ± 19	-49 ± 16	-30 ± 8
Archive ASW MCA Ref. 4-5	NA	NA	-99 ± 9
5 M $CaCl_2$, 90°C			
Current PCA Mockup (Table 2)	-124 ± 43	-121 ± 68	NA
Archive MA MCA Ref. 5	-182 ± 7	-121 ± 63	NA
Archive ASW MCA Ref. 5	-175 ± 10	-174 ± 15	-130 ± 3
6 m NaCl + 0.9 m KNO_3, 100°C			
Current PCA Mockup (Table 2)	-43 ± 13	-75 ± 1	NA
Archive ASW MCA Ref. 6	-49 ± 27	-63 ± 23	NA
MCA = Multiple Crevice Assembly (lollipop), ER,CREV obtained using the Tsujikawa-Hisamatsu Electrochemical (THE) Method (Ref. 4-5)			

4. Effect of Surface Black Annealing Oxide Film

4.1. Introduction

The effect of the presence of a black anneal oxide film on the surface of the test specimens was studied under the FY04 technical work plan (TWP) AWPT24. Testing was directed by Gabriel O. Ilevbare and Tammy Summers. The electrochemical tests were carried out by Robert A. Etien and Steve R. Gordon. The experimental details of this work are documented in SN-LLNL-SCI-463-V3, pages 85-100. The data is in TDMS under DTN LL040905212251.120 for acquired data and LL050501012251.033 and LL050502412251.144 for developed data.

Alloy 22 (N06022) is nickel (Ni) based and contains nominally 22% Chromium (Cr), 13% Molybdenum (Mo) and 3% tungsten (W). [1] Alloy 22 belongs to the Ni-Cr-Mo family of nickel based alloys, which also include alloys such as C-4 (N06455), C-276 (N10276), C-2000 (N06200), 59 (N06059) and 686 (N06686). [1] The Ni-Cr-Mo alloys were designed to withstand the most aggressive industrial applications, including reducing acids such as hydrochloric and oxidizing acids such as nitric. Chromium is the beneficial alloying element added for protection against oxidizing conditions and molybdenum is the beneficial alloying element to protect against reducing conditions. [2-4] The base element (nickel) protects the alloy against caustic conditions. [2-4] All three elements, Ni, Cr and Mo act synergistically to provide resistance to environmentally assisted cracking in hot concentrated chloride solutions. [2-4] The alloying elements Cr and Mo also provide resistance to localized corrosion such as pitting and crevice corrosion in chloride containing solutions. Some of the Ni-Cr-Mo alloys also contain a small amount of tungsten (W), which may act in a similar way as Mo regarding protection against localized corrosion. [5] Ni-Cr-Mo alloys are practically immune to pitting corrosion but they may suffer crevice corrosion under aggressive environmental conditions. The presence of oxyanions in the electrolyte inhibits crevice corrosion. [6-8] These oxyanions include mainly nitrate, sulfate and carbonate. [8-9] Fluoride ions also may inhibit crevice corrosion in Alloy 22. [10] A minimum ratio of inhibitor to chloride is needed for the inhibition to occur. [6-10]

Due to its excellent resistance to all forms of corrosion, Alloy 22 (N06022) has been selected to fabricate the external shell of the Yucca Mountain high-level nuclear waste containers. [11] The fabrication of the containers involves the rolling of plates into shape and then producing circumferential and longitudinal welds. Before inserting the nuclear waste into the container, these will be fully solution annealed to homogenize the microstructure and composition of the weld seams and to relieve residual stresses that might have been introduced during welding. [11] The method of solution annealing or solution heat treatment (SHT) will be in an uncontrolled atmosphere (in air). This is generally called black annealing since a black (and greenish) oxide scale grows on the exposed surfaces of the material. After heating at temperature for a specified time, the containers will be cooled down rapidly using water (water quenching). [11] The rapid cooling is necessary to avoid the precipitation of detrimental second phases in Alloy 22.

It has been shown that the corrosion rate of black annealed creviced specimens decreased with time when it was exposed to aerated chloride and nitrate containing solutions at 100°C. [12] Even though the corrosion rate of black annealed specimens was slightly more erratic than that

of freshly polished specimens, the corrosion rates of both types of specimens were in the order of only 50 nm/year after 100 days exposure. [12] The objective of this study was to investigate the influence of the black annealed oxide film for its resistance to crevice corrosion as compared to freshly polished specimens. The current work shows results comparing the repassivation potential of freshly polished creviced Alloy 22 specimens and specimens that were SHT in air at 2050°F (1121°C) for 20 min. and then water quenched.

Keywords: N06022, Black Annealing, Solution Heat Treatment, Chloride, Temperature, Corrosion Rate, Crevice Corrosion

4.2. Experimental

The specimens were machined from 1.25-inch thick plates (~32 mm). Table 4.1 shows the chemical composition of the material. The specimens were in the form of multiple crevice assemblies (MCA) or lollipops (Figure 4.1). The dimensions of the MCA were approximately 2 mm thick and a minimum of 11 cm long. The test part of the specimen was an annulus of 20 mm outside diameter and 7 mm inside diameter. The exposed surface area of each specimen was 7.43 cm². This surface area included the area covered by the crevice formers, which was 1.5 cm². The crevice formers were mounted on both sides of the specimen (Figure 4.1). Each crevice former consisted of a washer made of a ceramic material containing 12 crevicing spots or teeth with gaps in between the teeth (ASTM G 48). [13] Before mounting them onto the metallic specimens, the CF were covered with PTFE tape to ensure a tight crevicing gap. [14-16] The specimens had a ground finish of 600grit paper. There are two types of specimens mentioned in this work: (1) The as-received wrought mill annealed (MA) and (2) the solution heat-treated (MA + SHT) which were annealed in air for 20 min at 1121°C and then water quenched. The latter specimens were finished with 600-grit paper before the heat treatment but the final black oxide film (BOF) formed as a consequence of annealing and water quenching was not disturbed prior to testing. The SHT specimens were black with slight tones of green, typical of high temperature formed chromium oxide. For the electrochemical testing the MCA specimens were partially immersed, that is, water line crossed the stem of the specimen (Figure 4.1).

Table 4.2 shows the composition of the six test solutions. Nitrogen (N_2) was purged through the solution at a flow rate of 100cc/min for 24 hours while the corrosion potential (E_{corr}) was monitored. Nitrogen bubbling was continued throughout all the electrochemical tests. The electrochemical tests were conducted in a one-liter, three-electrode, borosilicate glass flask (ASTM G 5). [13] A water-cooled condenser combined with a water trap was used to avoid evaporation of the solution and to prevent the ingress of air (oxygen). The temperature of the solution was controlled by immersing the cell in a thermostatisized silicone oil bath, which was kept at a constant temperature. All the tests were carried out at ambient pressure. The reference electrode was saturated silver chloride (SSC) electrode, which has a potential of 199 mV more positive than the standard hydrogen electrode (SHE). The reference electrode was connected to the solution through a water-jacketed Luggin probe so that the electrode was maintained at near ambient temperature. The counter electrode was a flag (40 cm^2) of platinum foil spot-welded to a platinum wire. All the potentials in this paper are reported in the SSC scale.

Basically the test sequence for each specimen consisted of three parts: (1) E_{corr} evolution as a function of time for 24 h, (2) Polarization Resistance (ASTM G 59) [13] three subsequent times and (3) Cyclic Potentiodynamic Polarization (CPP) (ASTM G 61). [13]

Polarization Resistance (ASTM G 59): Corrosion rates (CR) were obtained using the polarization resistance method (ASTM G 59). Each one of these tests lasts approximately four minutes. An initial potential of 20 mV below the corrosion potential (E_{corr}) was ramped to a final potential of 20 mV above E_{corr} at a rate of 0.167 mV/s. Linear fits were constrained to the potential range of 10 mV below E_{corr} to 10 mV above E_{corr} putting the potential (independent variable) in the X-axis. The linear fit produces a value of slope, which is the resistance to polarization R_p. The Tafel constants, b_a and b_c, were assumed to be $\pm$ 0.12 V/decade. Corrosion rates were calculated using Equation 1

$$i_{corr} = \frac{1}{R_p} \cdot \frac{b_a \cdot b_c}{2.303(b_a + b_c)} \ldots and \cdots CR(\mu m / yr) = k \frac{i_{corr}}{\rho} EW \qquad (4.1)$$

Where k is a conversion factor, i_{corr} is the calculated corrosion current density in A/cm^2 (using values of the slope R_p in V/A), EW is the equivalent weight, and ρ is the density of Alloy 22 (8.69 g/cm^3). Assuming an equivalent dissolution of the major alloying elements as Ni^{2+}, Cr^{3+}, Mo^{6+}, Fe^{2+}, and W^{6+}, the EW for Alloy 22 is 23.28 (ASTM G 102). [13]

Cyclic Potentiodynamic Polarization - CPP (ASTM G 61): The cyclic potentiodynamic polarization technique, CPP (ASTM G 61) [13] is one of the tests commonly used to assess the susceptibility of Alloy 22 to localized corrosion and its passive stability. The potential scan was started 150 mV below E_{corr} at a set scan rate of 0.167 mV/s. The scan direction was reversed when the current density reached 5 mA/cm^2 in the forward scan. Depending on the range of applied potentials, each CPP test could last between 1 h and 3 h. After the CPP tests, the specimens were examined in an optical stereomicroscope at a magnification of at least 20 times to establish the mode and location of the attack.

4.3. Results

4.3.1. The Corrosion Potential (Ecorr) and the Corrosion Rate (CR)

Tables 4.3, 4.4 and 4.5 show the values of the corrosion potential (E_{corr}) and the corrosion rate (CR) of MA and SHT specimens after 24-h immersion in the deaerated electrolytes. The values of E_{corr} and CR in Tables 4.3, 4.4 and 4.5 are for comparative purposes only and do not represent steady state values. That is, the values of E_{corr} and CR in Tables 4.3, 4.4 and 4.5 are not the values at which Alloy 22 would ultimately corrode when exposed to similar environments in aerated conditions for exposure times longer than 24-h. In general, Tables 4.3, 4.4 and 4.5 show that the E_{corr} of the MA specimens was lower than that of the SHT specimens. This suggests that the high temperature air formed oxide film (SHT) provided some protection in the respective electrolyte solutions during the early immersion times. Figure 4.2 and Table 4.3 show the 24-h corrosion rates for Alloy 22 in deaerated 5 M $CaCl_2$ solution at 60°C and 90°C. For both types of specimens the corrosion rate was slightly higher for the higher temperature. It

is also apparent that the corrosion rate of the SHT specimens was lower than that of the MA specimens, again suggesting that the high temperature air formed oxide film provided early protection against corrosion in these environments. Figure 4.2 also shows that the corrosion rate slightly increased as the temperature increased. Figure 4.3 shows the 24-h corrosion rates for Alloy 22 in deaerated 6 m NaCl + 0.3 and 0.9 m KNO_3 solution at 80°C and 100°C. Again, similarly as in 5 M $CaCl_2$ (Figure 4.1) it is apparent that the corrosion rate of the SHT specimens was lower than that of the MA specimens, also suggesting that the high temperature air formed oxide film provided early protection against corrosion in these environments. The remaining CR data in Tables 4.3, 4.4 and 4.5 show in general a similar behavior, that is, the corrosion rate of the SHT specimens was lower than that of the MA specimens. Most of the corrosion rates in Tables 4.3, 4.4 and 4.5 are between 0.1 μm/year and 1 μm/year. It is expected that the corrosion rate of Alloy 22 will decreased as the exposure time in the electrolytes increases. [12,17-16] It is also expected that the E_{corr} values in Tables 4.3, 4.4 and 4.5 will increase as a function of time. The rate of increase and the final steady-state value will depend on the composition, pH and temperature of the electrolyte. The presence of oxygen in the electrolyte will also control the rate of increase of E_{corr}.

4.3.2. Cyclic Potentiodynamic Polarizations (CPP)

Figure 4.4 shows the cyclic potentiodynamic polarization curves for individual Alloy 22 specimens in deaerated 5 M $CaCl_2$ solutions at 60°C. Figure 4.4 shows that the polarization curve of the SHT specimen was different from the polarization curve for the MA polished specimen. Basically, the MA specimen can be polarized to higher potentials and the curve does not show hysteresis during the reverse scan. It is apparent that the SHT specimen can produce more output current for the same initial applied potential up to 200 mV SSC than the MA polished specimen. It is likely that the oxide scale in the SHT specimen reacts with the electrolyte providing the additional current. After the CPP tests, the SHT specimens showed attack on the bold surfaces of the specimen, while the MA polished specimen showed minimal dull crevice corrosion even though the latter was polarized to 1 V or five times higher than the SHT specimens (Table 4.6). Figure 4.4 also shows that corrosion potential for the SHT specimen was higher than for the MA specimen and that the passive current density for the SHT specimen was lower than for the MA polished specimen. This confirms the findings discussed in the previous section.

Figure 4.5 shows the CPP curves for both types of specimen in 5 M $CaCl_2$ at 90°C. While the passive current density for the SHT specimen was lower than for the MA specimen, their breakdown potential and repassivation potentials were similar. Table 4.6 shows that the mode of attack after the CPP was different for these two types of specimens.

Figure 4.6 shows the CPP curves for both types of specimen in 6 m NaCl + 0.9 m KNO_3 solution at 100°C. Even though the SHT specimen had an initially higher corrosion potential, the full anodic behavior and the repassivation potential for both type of specimens was similar. Both curves show a hysteresis in the reverse scan suggesting the presence of localized corrosion. Table 4.6 shows that both types of specimens suffered crystallographic crevice corrosion.

4.3.3. Parameters from the Anodic Polarization Curves

In a cyclic potentiodynamic polarization (CPP) curves (e.g. Figures 4.4-4.6) there are several typical potentials. They can be divided in two groups: (1) Breakdown potentials in the forward scan, called E20 and E200 that represent the potential that needs to be applied to the specimen in the forward scan for the current density to reach respectively 20 μA/cm² and 200 μA/cm². (2) Repassivation potentials in the reverse scan, called ER10, ER1 and ERCO. ER10 and ER1 represent the potential that needs to be applied in the reverse scan for the current density to reach 10 μA/cm² and 1 μA/cm², respectively. ERCO represents the potential at which the reverse scan crosses over (CO) the forward scan in the passive region of potentials. [8,9,16,19-21] That is, in the forward scan, when the current density reaches for example 200 μA/cm² in the forward scan it can be considered that the alloy has lost its passive mode and that when the current density in the reverse scan has reached 1 μA/cm², the alloy has regained its passive behavior prior to the breakdown. Tables 4.3-4.5 list these parameters for both types of specimen in the six investigated electrolytes. Tables 4.3-4.5 show that the value of ER1 to indicate repassivation is always available from a CPP curve; however ERCO values only exist when the intersection occurs, that is, in presence of an obvious hysteresis.

Figure 4.7 shows the parameters from the CPP (Table 4.3) for the tests carried out in 1 M NaCl solution at 90°C. The 24-h E_{corr} values are also shown. Figure 4.7 shows that the anodic behavior of Alloy 22 was practically the same for both types of specimens. The breakdown potentials (E20 and E200) are practically identical between SHT and MA specimens. The repassivation potentials (ER10, ER1 and ERCO) of the SHT specimens are slightly higher than those of the MA specimens. Table 4.6 shows that both type of specimens suffered crystallographic crevice corrosion after the CPP tests.

Figure 4.8 shows the repassivation potential (ER1) for the specimens tested in solutions containing 6 m NaCl plus two different amounts of KNO_3, both at 80°C and 100°C. In both solutions, at both temperatures ER1 for the SHT specimens was higher than for the MA specimens, suggesting higher resistance to localized corrosion. Table 4.6 shows that the mode of attack of both types of specimens was similar in each tested conditions. At the lower temperature (80°C) and at the higher nitrate to chloride ratio (0.15), the attack in the SHT specimen seems slightly more pronounced than in the MA specimens. This is mainly due to a larger amount of crevice corrosion and pitting like corrosion in the bold surfaces.

Figure 4.9 shows the repassivation potential (ER1) for the specimens tested in 3.5 m NaCl + 0.525 m KNO_3 at 60°C and 100°C and in 0.1 m NaCl + 0.001 m $NaHCO_3$ at 60°C and 95°C. In general, the repassivation potentials for the MA specimens were lower than for the SHT specimens. For the NaCl + KNO_3 solution at 100°C the repassivation potentials were practically the same for both types of specimens. Figure 4.10 shows the repassivation potentials for two chloride concentrations and for fixed ratio of nitrate over chloride at 100°C. At the lower chloride concentration the repassivation potential of the SHT specimens was slightly lower than for the MA specimens, but this trend was reversed at the higher chloride concentration. Figure

4.10 also shows that there is very little influence of the total concentration of chloride for this studied range.

4.3.4. Type of Attack in the Specimens after Anodic Polarization

Table 4.6 shows a description of the attack in the specimens after the CPP tests. In general, for both SHT and MA specimens, the mode of attack was the same, especially in the most aggressive conditions such as at the higher temperatures and lower nitrate to chloride ratios. For example in the 1 M NaCl solution at 90°C, the main mode of attack was crystallographic crevice corrosion for both types of specimens (Figures 4.11 and 4.12). Similarly in the 6 m NaCl + 0.3 m KNO_3 at 100°C, the main mode of attack for both types of specimens was also crevice corrosion (Figures 4.13 and 4.14). In 5 m $CaCl_2$ at 90°C, the attack was outside the crevice former, on the flat face of the specimen for the MA condition and on the edge and borders for the SHT specimens (Figures 4.15 and 4.16). In the less aggressive environments (lower temperatures and higher nitrate to chloride ratio) the mode of attack was slightly different for both types of specimens. In the pure chloride solutions (1 M NaCl and 5 M $CaCl_2$) at 60°C the attack in the MA specimens was mostly transpassivity and dull crevice corrosion. However, for the SHT specimens, the main attack was boldly pitting corrosion type of attack. Similarly for the 6 m NaCl + 0.9 m KNO_3 at 80°C, the attack in the MA specimens was transpassivity and dull crevice corrosion while in the SHT specimens the attack was crystallographic crevice corrosion and pitting like in the bold areas. Figures 4.17 and 4.18 show the mode of attack in 0.1 m NaCl + 0.001 m $NaHCO_3$ solution at 95°C for MA and SHT specimen respectively. For the MA specimen the attack is uniform mostly dull crevice corrosion around the rim of the crevice former. For the SHT specimen the attack is partly crystallographic crevice corrosion and partly edge and border attack. In 0.1 m NaCl + 0.001 m $NaHCO_3$ solution at 60°C (Figures 4.19 and 4.20) the attack in the MA specimen is mostly transpassivity and in the SHT specimen border attack.

4.3.5. Concluding Remarks

Cyclic polarization curves have been carried out to determine the effect of the solution heat treated (SHT) high temperature oxide scale on the resistance of Alloy 22 to localized corrosion. To assess the effect of the black oxide film tests were performed in parallel using mill annealed (MA) specimens which were freshly polished to provide a more or less oxide free surface. The tests were carried out in a variety of environments from pure chloride solutions (such as 5 m $CaCl_2$) to solutions that contained chloride plus the inhibitive nitrate oxyanion (such as 6 m NaCl + 0.9 m KNO_3). Tests were also carried out in dilute solutions such as 0.1 m NaCl + 0.001 m $NaHCO_3$. The test solutions had a range of pH from 4.7 to 8. The test temperature ranged from 60°C to 100°C. In most of the tested conditions, the SHT specimens had similar repassivation potential as the MA specimens. Additionally, in most cases, the repassivation potential for the SHT specimens were slightly higher than for the MA specimens. A higher repassivation potential indicates a higher resistance to localized corrosion. The mode of attack of the MA and SHT materials was also similar. In cases of low environmental aggressiveness the

mode of attack varied slightly between MA and SHT specimens; however the metrics (repassivation potential values) remained practically the same.

Under the tested conditions it does not seem to be a detrimental effect of the black annealing oxide scale on the resistance of Alloy 22 to localized corrosion.

Another report (Sharon Torres et al.) compares the effect of annealing temperature on the resistance to localized corrosion of Alloy 22 welds. The comparison was done using freshly polished specimens. As the annealing temperature increased, the crevice repassivation potential slightly increased in 1 M NaCl at 90°C. That is, it appears that solution annealing has a beneficial effect on the resistance to localized corrosion of Alloy 22 welds. Similar beneficial effect of annealing was found in specimens tested in 6 m NaCl + 0.9 m KNO_3 at 100°C.

4.4. Conclusions

1. The short-term (24-h) E_{corr} of Alloy 22 in deaerated solutions was generally higher for the SHT specimens than for the MA specimens.

2. The short-term corrosion rate in deaerated electrolytes was generally lower for the SHT than for the MA specimens.

3. The repassivation potentials for the SHT specimens were comparable to the MA specimens. In many cases the repassivation potential of the SHT specimens was slightly higher than for the MA specimens.

4. The mode of localized corrosion attack of the SHT and MA was practically the same. When the tested conditions were less aggressive (for example at the lower temperatures) the mode of attack between the two types of specimens varied slightly.

4.5. References

1. ASTM International, Annual Book of ASTM Standards, Volume 02.04 "Non-Ferrous Metals" Standard 575 B (West Conshohocken, PA: ASTM International, 2002)
2. R. B. Rebak and P. Crook, Transportation, Storage and Disposal of Radioactive Materials, PVP-Vol. 483, p. 131 (American Society of Mechanical Engineers, 2004: New York, NY)
3. R. B. Rebak in Corrosion and Environmental Degradation, Volume II, p. 69 (Wiley-VCH, 2000: Weinheim, Germany)
4. R. B. Rebak and P. Crook, *Advanced Materials and Processes*, February 2000
5. R. B. Rebak and P. Crook, Proceeding of the Symposium Critical Factors in Localized Corrosion III, PV 98-17, p. 289 (The Electrochemical Society, 1998: Pennington, NJ)
6. G. A. Cragnolino, D. S. Dunn and Y.-M. Pan "Localized Corrosion Susceptibility of Alloy 22 as a Waste Package Container Material," Scientific Basis for Nuclear Waste Management XXV, Vol. 713, p. 53 (Materials Research Society 2002: Warrendale, PA)
7. D. S. Dunn, L. Yang, C. Wu and G. A. Cragnolino, Mat. Res. Soc. Symp. Proc. Vol 824 (MRS, 2004: Warrendale, PA)
8. J. H. Lee, T. Summers and R. B. Rebak, Paper 04692, Corrosion/2004 (NACE International, 2004: Houston, TX)
9. R. B. Rebak, Paper 05610, Corrosion/2005 (NACE International, 2005: Houston, TX)
10. R. M. Carranza, M. A. Rodríguez and R. B. Rebak, "Inhibition of Chloride Induced Crevice Corrosion in Alloy 22 by Fluoride Ions," Paper 06626, Corrosion/2006 (NACE International, 2006: Houston, TX)
11. G. M. Gordon, Corrosion, 58, 811 (2002)
12. K. J. King, J. C. Estill, G. A. Hust, M. L. Stuart and R. B. Rebak, Paper 05607, Corrosion/2005 (NACE International, 2005: Houston, TX)
13. ASTM International, Annual Book of ASTM Standards, Volume 03.02 "Wear and Erosion; Metal Corrosion" G-15, G-61, etc. (West Conshohocken, PA: ASTM International, 2004)
14. K. J. Evans, S. D. Day, G. O. Ilevbare, M. T. Whalen, K. J. King, G. A. Hust, L. L. Wong, J. C. Estill and R. B. Rebak, Transportation, Storage and Disposal of Radioactive Materials, PVP-Vol. 467, p. 55 (American Society of Mechanical Engineers, 2003: New York, NY)
15. G. O. Ilevbare, K. J. King, S. R. Gordon, H. A. Elayat, G. E. Gdowski and T. S. E. Summers "Effect of Nitrate on the Repassivation Potential of Alloy 22 in Chloride Containing Solutions," Fall 2004 Meeting of the Electrochemical Society, 0308Oct04, Honolulu, HI (to be published)
16. B. A. Kehler, G. O. Ilevbare and J. C. Scully, Corrosion, p. 1042 (2001)
17. K. J. Evans and R. B. Rebak in Corrosion Science – A Retrospective and Current Status in Honor of Robert P. Frankenthal, PV 2002-13, p. 344-354 (The Electrochemical Society, 2002: Pennington, NJ).

18. R. M. Carranza, M. A. Rodríguez and R. B. Rebak, "Passivity of Alloy 22 in Chloride and Fluoride Containing Solutions," Paper 06-02, 16th International Corrosion Congress, Beijing, China 19-24 September 2005.
19. K. J. Evans, A. Yilmaz, S. D. Day, L. L. Wong, J. C. Estill and R. B. Rebak "Comparison of Electrochemical Methods to Determine Crevice Corrosion Repassivation Potential of Alloy 22 in Chloride Solutions," JOM, January 2005 (TMS, 2005: Warrendale, PA)
20. D. S. Dunn and C. S. Brossia, Paper 02548, Corrosion 2002 (NACE International, 2002: Houston, TX)
21. K. J. Evans, L. L. Wong and R. B. Rebak, Transportation, Storage and Disposal of Radioactive Materials, PVP-Vol. 483, p. 137 (American Society of Mechanical Engineers, 2004: New York, NY)

Table 4.1 -
Chemical Composition in weight % of the tested Specimens. All Specimens in the Wrought Condition (Non-Welded).

Specimens/Element	Ni	Cr	Mo	W	Fe	Others
Nominal ASTM B 575	50-62	20-22.5	12.5-14.5	2.5-3.5	2-6	2.5Co-0.5Mn-0.35V (A)
DEA Specimens Heat 2277-1-3265	~57	21.2	12.9	2.5-3.5	3.9	0.7Co-0.25Mn-0.17V
JE Specimens Heat 059902LL1	59.56	20.38	13.82	2.64	2.85	0.17V-0.16Mn

(A) Maximum

Table 4.2 – Test Solutions

Test Solution	$[NO_3^-]/[Cl^-]$	Ambient pH	Test Temperature (°C)
1 M NaCl	0	6.1	60, 90
5 M $CaCl_2$	0	4.7	60, 90
6 m NaCl + 0.9 m KNO_3	0.15	6.2	80, 100
6 m NaCl + 0.3 m KNO_3	0.05	6.3	80, 100
3.5 m NaCl + 0.525 m KNO_3	0.15	6.7	60, 100
0.1 m NaCl + 0.001 m $NaHCO_3$	0.01 *	8.0	60, 95
	* $[HCO_3^-]/[Cl^-]$		

Table 4.3 – Characteristic Potentials (mV SS) and Corrosion Rates (μm/year) for Alloy 22

Specimen ID	Type of Specimen	E_{corr}, 24 h (mV, SSC)	Corrosion Rates (μm/year) after 24-h	E20 (mV, SSC)	E200 (mV, SSC)	ER10 (mV, SSC)	ER1 (mV, SSC)	ERCO (mV, SSC)
5 M $CaCl_2$, 60°C, pH 4.7								
DEA3375	MA 600	-267	0.2469, 0.5714	(2 AP) 876	978	837	694	None (80 AP)
DEA3387	MA 600	-360	2.111, 1.123, 3.055	(-63 AP) 897	1000	861	728	None
DEA3369	SHT	-278	0.1361, 0.1551, 0.1443	61	105	-43	-115	-163
DEA3368	SHT	-194	0.0993, 0.0793, 0.1016	84	126	-40	-111	-164
5 M $CaCl_2$, 90°C, pH 4.7								
DEA3376	MA 600	-319	1.3430, 0.8258, 0.9245	-22	78	-163	-185	-183
DEA3388	MA 600	-354	3.4470, 3.6540, 3.2220	-130	76	-123	-180	-35
DEA3370	SHT	-309	0.2334, 0.2282, 0.2469	25	50	-99	-156	-200
DEA3371	SHT	-189	0.5906, 0.5273, 0.5534	27	51	-111	-165	-185
1 M NaCl, 60°C, pH 6.1								
JE3321	MA 600	-456	0.244, 0.279, 0.317	723	797	628	163	84 MH
JE3322	MA 600	-579	1.633, 1.045, 1.157	697	819	668	65	28
JE3301	SHT	-387	0.286, 0.276, 0.303	479	935	185	17	-10
JE3302	SHT	-390	0.267, 0.279, 0.274	317	908	140	-4	77
1 M NaCl, 90°C, pH 6.1								
JE3324	MA 600	-593	2.413, 2.117, 2.300	261	438	-38	-117	-126
JE3328	MA 600	-484	0.422, 0.438, 0.443	228	475	-33	-113	-109
JE3303	SHT	-254	0.257, 0.251, 0.244	307	448	94	-39	-80
JE3304	SHT	-412	0.268, 0.277, 0.282	179	422	78	-13	66
MA 600 = As received wrought specimens finished with paper 600 (polished), SHT = Solution heat-treated specimens containing the black annealed oxide film (BOF) on the surface (1121°C for 20 min plus water quenched). MH = Minor or no hysteresis								

Table 4.4 – Characteristic Potentials (mV SS) and Corrosion Rates (μm/year) for Alloy 22

Specimen ID	Type of Specimen	$E_{corr,}$ 24 h (mV, SSC)	Corrosion Rates (μm/year) After 24-h	E20 (mV, SSC)	E200 (mV, SSC)	ER10 (mV, SSC)	ER1 (mV, SSC)	ERCO (mV, SSC)
6 m NaCl + 0.9 m KNO_3, 80°C (NO_3^-/Cl^- = 0.15), pH 6.2								
JE3317	MA 600	-501	0.301, 0.279, 0.256	637	810	635	9	-52
JE3318	MA 600	-471	0.304, 0.235, 0.398	649	800	624	-8	-27
JE3309	SHT	-371	0.0803, 0.0804, 0.0816	769	909	101	-6	-12
JE3310	SHT	-257	0.158, 0.160, 0.160	756	917	134	13	-25
6 m NaCl + 0.9 m KNO_3, 100°C (NO_3^-/Cl^- = 0.15) , pH 6.2								
JE3319	MA 600	-460	0.558, 0.301, 0.308	430	737	-6	-77	-84
JE3320	MA 600	-486	3.663, 3.841, 3.643	527	777	-8	-82	-88
JE3311	SHT	-303	0.411, 0.341, 0.380	362	843	16	-15	-11
JE3312	SHT	-316	0.274, 0.274, 0.258	480	863	14	-41	-48
6 m NaCl + 0.3 m KNO_3, 80°C (NO_3^-/Cl^- = 0.05) , pH 6.3								
JE3313	MA 600	-515	0.3815, 0.5266, 0.3599	437	832	-20	-103	-114
JE3314	MA 600	-494	0.3397, 0.3234, 0.3095	465	814	-29	-99	-107
JE3305	SHT	-200	0.2099, 0.2242, 0.2513	368	874	40	-17	-31
JE3306	SHT	-270	0.0883, 0.0894, 0.0816	438	893	43	-1	-10
6 m NaCl + 0.3 m KNO_3, 100°C (NO_3^-/Cl^- = 0.05) , pH 6.3								
JE3315	MA 600	-259	0.6496, 0.5996, 0.8536	278	402	-47	-84	-88
JE3316	MA 600	-533	0.7197, 0.704, 0.6882	211	315	-53	-78	-79
JE3307	SHT	-237	0.1971, 0.1721, 0.1951	140	420	5	-12	-14
JE3308	SHT	-243	0.2998, 0.2647, 0.2911	270	437	14	-5	-6
MA 600 = As received wrought specimens finished with paper 600 (polished), SHT = Solution heat-treated specimens containing the black annealed oxide film (BOF) on the surface (1121°C for 20 min plus water quenched). MH = Minor or no hysteresis								

Table 4.5 – Characteristic Potentials (mV SS) and Corrosion Rates (μm/year) for Alloy 22

Specimen ID	Type of Specimen	$E_{corr,}$ 24 h (mV, SSC)	Corrosion Rates (μm/year) After 24-h	E20 (mV, SSC)	E200 (mV, SSC)	ER10 (mV, SSC)	ER1 (mV, SSC)	ERCO (mV, SSC)
3.5 m NaCl + 0.525 m KNO_3, 60°C (NO_3^-/Cl^- = 0.15), pH 6.7								
DEA3383	MA 600	-293	0.1567, 0.08791, 0.1884	571	NA (A)	431	327	331 MH
DEA3384	MA 600	-170	0.5439, 0.557, 0.5548	NA (A)	NA (A)	440	288	364 MH
DEA3389	MA 600	-456	0.245, 0.295, 0.1557	(-128) AP, 596	854	629	336	808 MH
DEA3360	SHT	-81	0.1735, 0.1768, 0.1645	NA (A)	NA (A)	NA (A)	447	-18 MH
DEA3361	SHT	-186	0.7529, 0.7233, 0.7829	339	NA (A)	162	-78	-162 MH
3.5 m NaCl + 0.525 m KNO_3, 100°C (NO_3^-/Cl^- = 0.15), pH 6.7								
DEA3385	MA 600	-340	0.2588, 0.2467	448	NA (A)	80	-74	-32 / -82
DEA3386	MA 600	-207	1.398, 1.548, 1.377	337	NA (A)	177	-8	111 MH
DEA3390	MA 600	-480	0.292, 0.5749, 0.7618	(-90) AP 425	682	333	-5	-81
DEA3362	SHT	-257	0.9688, 0.9592, 0.8437	NA (A)	NA (A)	NA (A)	-71	-198 MH
DEA3363	SHT	-222	1.332, 1.284, 1.279	234	NA (A)	74	-69	-72
DEA3374	SHT	-316	1.291, 1.172, 1.527	742	930	76	-20	-2
0.1 m NaCl + 0.001 m $NaHCO_3$, 60°C (HCO_3^-/Cl^- = 0.01), pH 8.0								
DEA3377	MA 600	-472	0.158, 0.1184, 0.1071	735	857	381	263	400
DEA3379	MA 600	-413	0.1378, 0.1358, 0.107	(3) AP	NA (A)	NA (A)	458	NA
DEA3380	MA 600	NA	0.2295, 0.2397, 0.1542	NA (A)	NA (A)	NA (A)	420	NA
DEA3364	SHT	-252	0.2188, 0.2328, 0.2308	NA (A)	NA (A)	NA (A)	380	80 MH
DEA3365	SHT	-280	0.0319, 0.0392, 0.0363	NA (A)	NA (A)	NA (A)	497	126 MH
DEA3372	SHT	-206	0.0673, 0.0909, 0.0784	726	NA	746	538	NA
0.1 m NaCl + 0.001 m $NaHCO_3$, 95°C (HCO_3^-/Cl^- = 0.01), pH 8.0								
DEA3378	MA 600	-252	0.1558, 0.4024, 0.6637	329	771	32	-100	-141
DEA3381	MA 600	-267	0.3985, 0.1288, 0.4037	325	NA (A)	8	-105	-141
DEA3382	MA 600	-226	0.3275, 0.4018, 0.4753	331	NA (A)	57	-86	-129
DEA3366	SHT	-297	0.0377, 0.0990, 0.090	NA (A)	NA (A)	NA (A)	543	NA
DEA3367	SHT	-246	0.1673, 0.1673, 0.1867	536	NA (A)	255	92	-168 MH
DEA3373	SHT	-403	0.2191, 0.234, 0.227	195	319	116	-193	-278
MA 600 = As received wrought specimens finished with paper 600 (polished), SHT = Solution heat-treated specimens containing the black annealed oxide film (BOF) on the surface (1121°C for 20 min plus water quenched). MH = Minor or no hysteresis, (A) The maximum applied potential was +600 mV SSC, AP = Anodic Peak								

Table 4.6 – Observations on the Crevice Specimens After the CPP Tests

Solution	T (°C)	Specimens	Observations
1 M NaCl	60	MA 600	Yellow TP. Small dull CC
		SHT	Crystallographic CC. Some pitting corrosion in bold areas.
	90	MA 600	TP. Crystallographic CC. Caked corrosion products under CF.
		SHT	Crystallographic CC. No bold TP
5 M $CaCl_2$	60	MA 600	Small dull CC
		SHT	Isolated pitting-like attack, attack on edges following lamination directions. No CC
	90	MA 600	Typical Massive attack in bold surface, starting at the CF and following gravity, attack on edges. No CC
		SHT	Edge attack following lamination directions, pitting-like attack, especially on corners. Stem edges attack. No CC
6 m NaCl + 0.9 m KNO_3	80	MA 600	Bold TP. Dull, minimal CC. Some crystallographic CC
		SHT	Crystallographic CC. Some pitting corrosion on bold surfaces.
	100	MA 600	TP in bold surfaces. Dull and deep crystallographic CC.
		SHT	Crystallographic CC. Bold TP.
6 m NaCl + 0.3 m KNO_3	80	MA 600	Iridescent TP. Dull and Shiny Crystallographic CC
		SHT	Black Specimen. Crystallographic CC, deep at spots
	100	MA 600	TP. Deep crystallographic CC in almost every CF spot
		SHT	Black. Crystallographic CC in almost every CF spot.
3.5 m NaCl + 0.525 m KNO_3	60	MA 600	Shiny, little or no TP. No CC. No Localized Corrosion
		SHT	Black. No discoloration. Little or no CC. Edge attack.
	100	MA 600	Iridescent blue/tan TP. Small dull CC.
		SHT	Black. Small spotty CC. Some edge attack
0.1 m NaCl + 0.001 m $NaHCO_3$	60	MA 600	Bluish/Tan TP. No CC.
		SHT	Black. Blue discoloration. No CC. Attack on borders
	95	MA 600	Bluish/Tan TP. Small dull CC around the rim of CFs
		SHT	Black/Bluish. Little CC. Edge and border attack.
TP = Transpassivity, CC = Crevice Corrosion, CF = Crevice Former (total of 24 spots)			

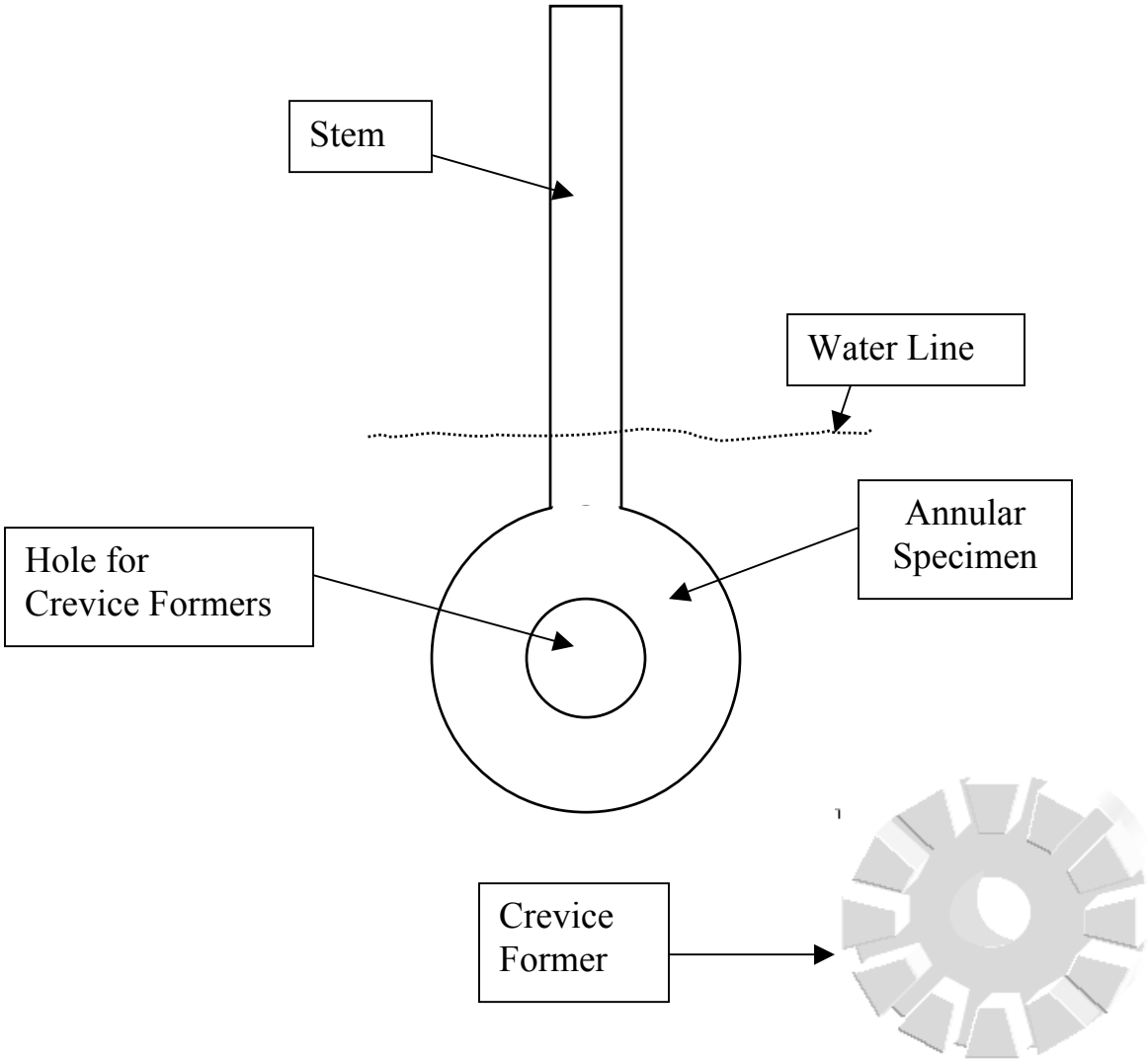

Figure 4.1 – Multiple Crevice Assembly (MCA) Specimen and Crevice Former (CF). Further photographs of the corroded specimens generally correspond to one quarter of the tested surface.

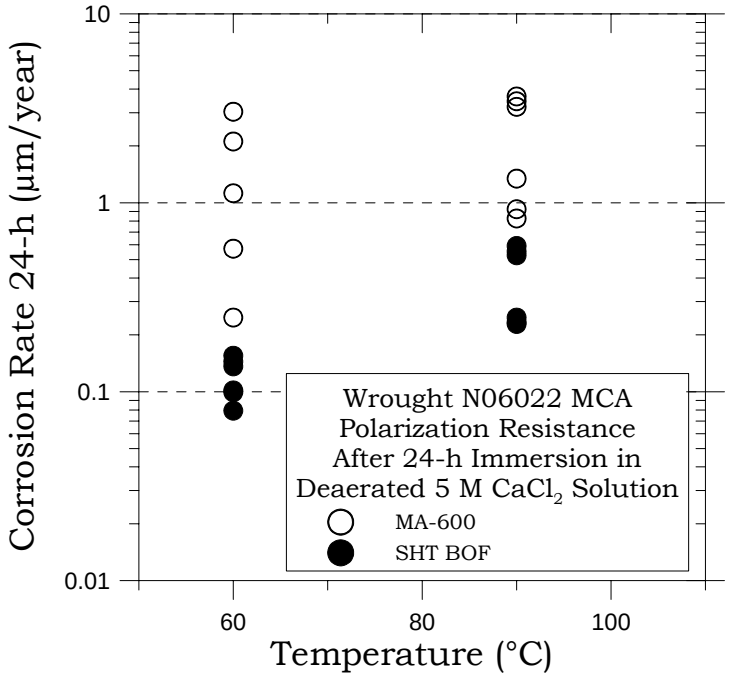

Figure 4.2 – CR for MA and SHT Alloy 22 Specimens in 5 M $CaCl_2$

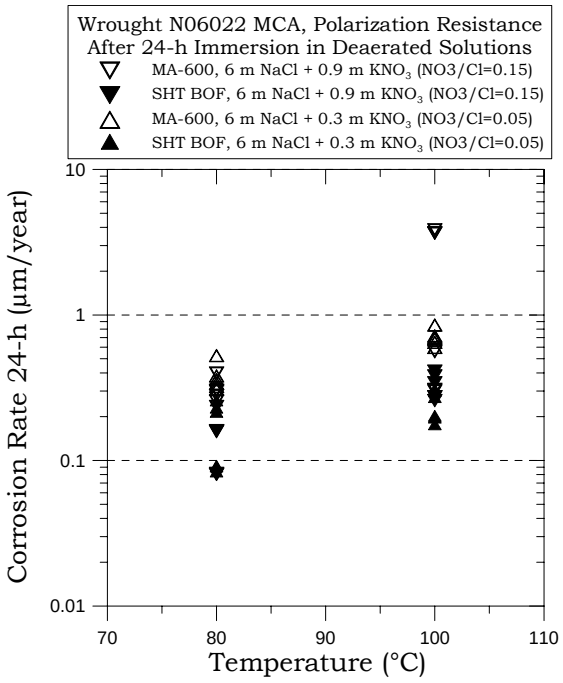

Figure 4.3 – CR for MA and SHT Alloy 22 Specimens in NaCl + KNO_3 Solutions

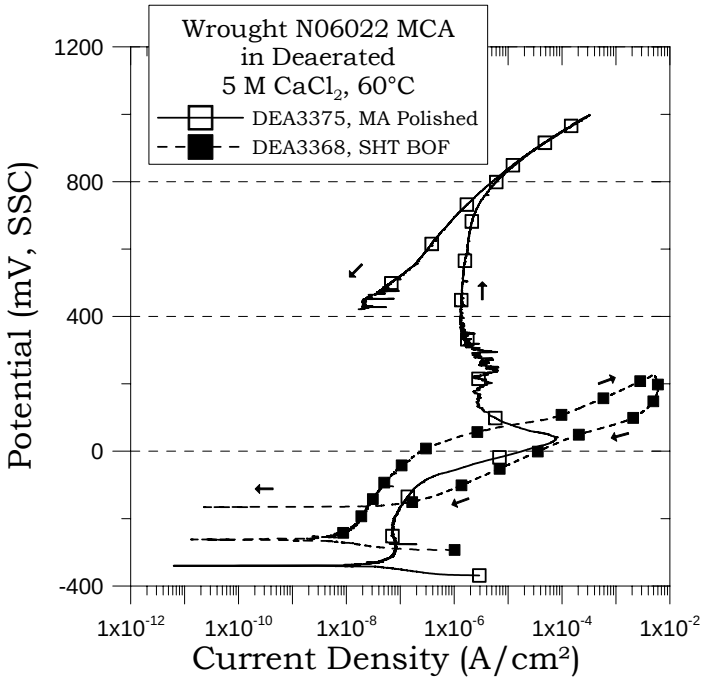

Figure 4.4 – Cyclic Potentiodynamic Polarization (CPP) for MA and SHT Alloy 22 Specimens in 5 M $CaCl_2$ at 60°C

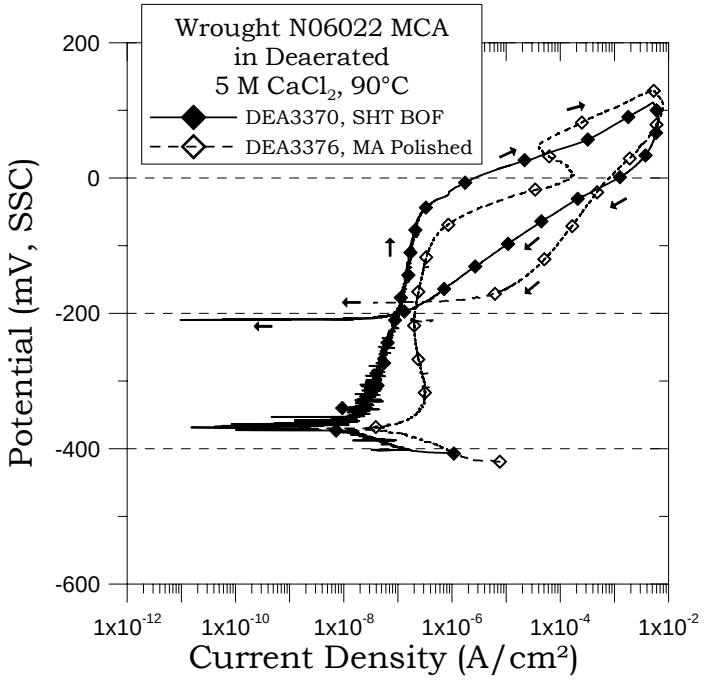

Figure 4.5 – CPP for MA and SHT Alloy 22 Specimens in 5 M $CaCl_2$ at 90°C

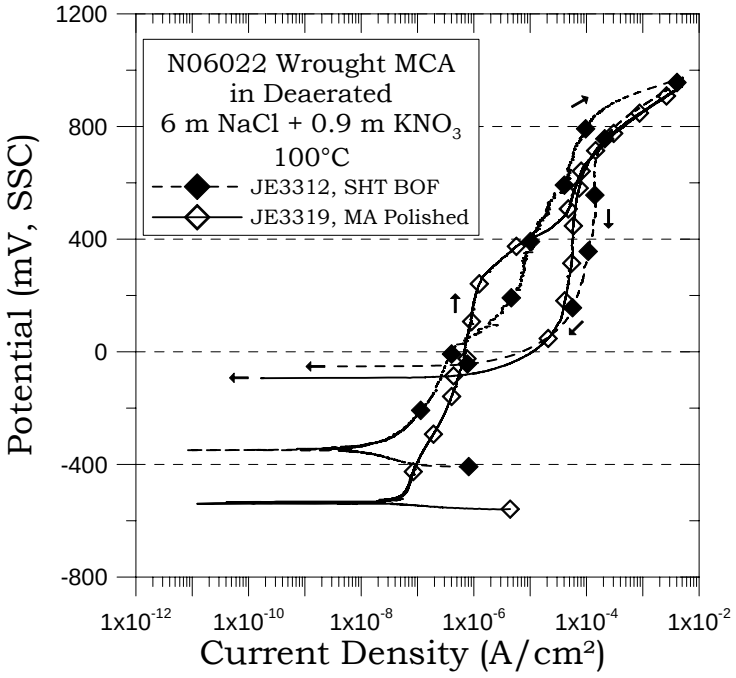

Figure 4.6 – CPP for MA and SHT Alloy 22 Specimens in 6 m NaCl + 0.9 m KNO_3 at 100°C

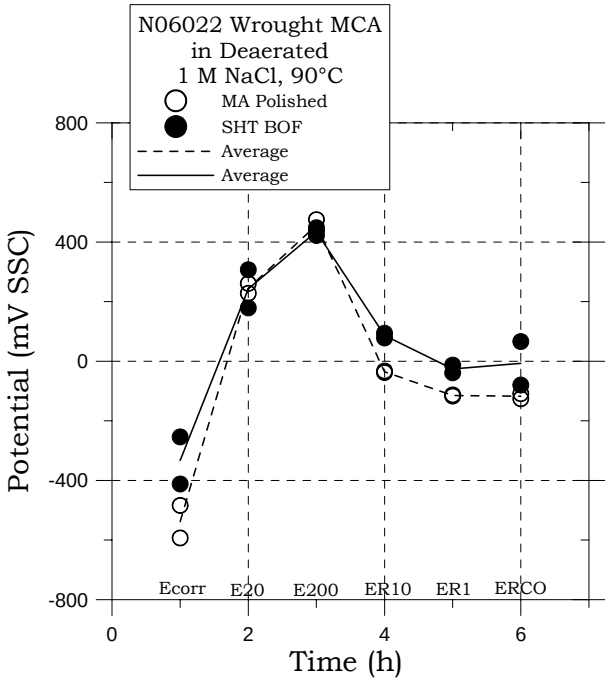

Figure 4.7 – Parameters from CPP for MA and SHT Alloy 22 in 1 M NaCl at 90°C

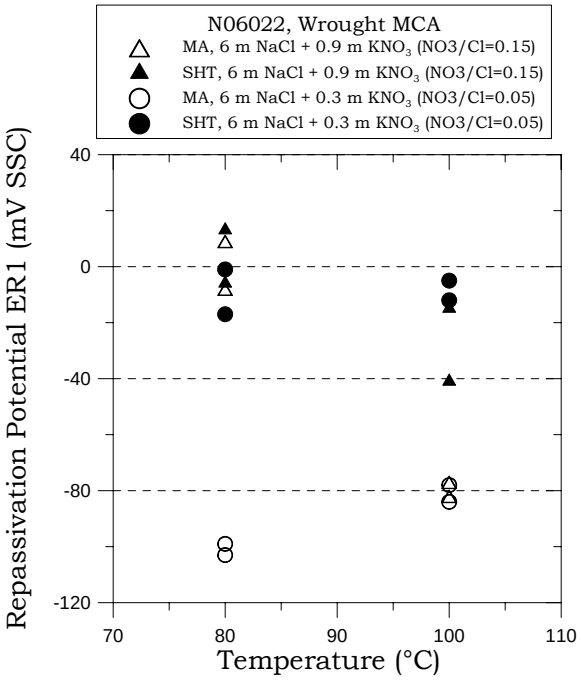

Figure 4.8 – ER1 for MA and SHT Alloy 22 Specimens in 6 m NaCl + 0.9 m KNO_3

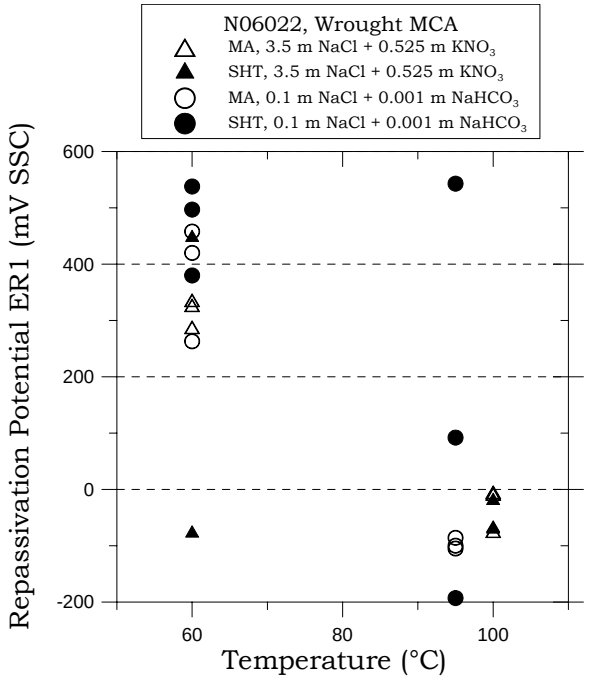

Figure 4.9 – ER1 for MA and SHT Alloy 22 Specimens in 3.5 m NaCl + 0.525 m KNO_3 and 0.1 m NaCl + 0.001 m $NaHCO_3$

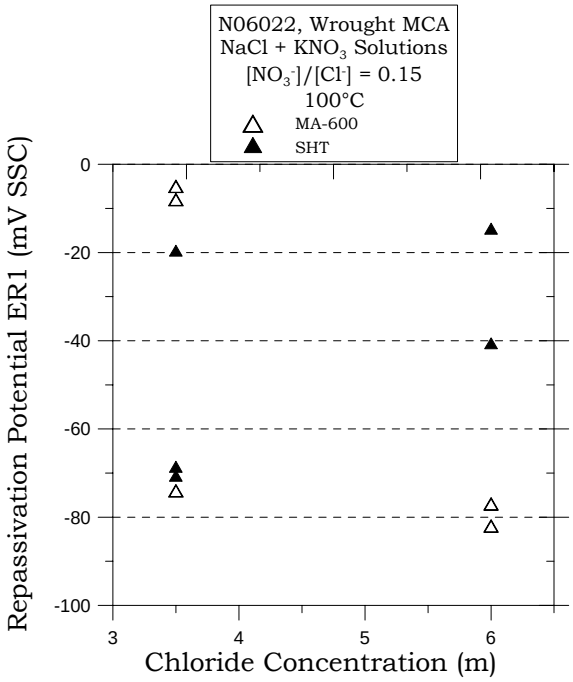

Figure 4.10 – ER1 for MA and SHT Alloy 22 Specimens in NaCl + KNO_3 solutions for a Nitrate over Chloride ratio of 0.15

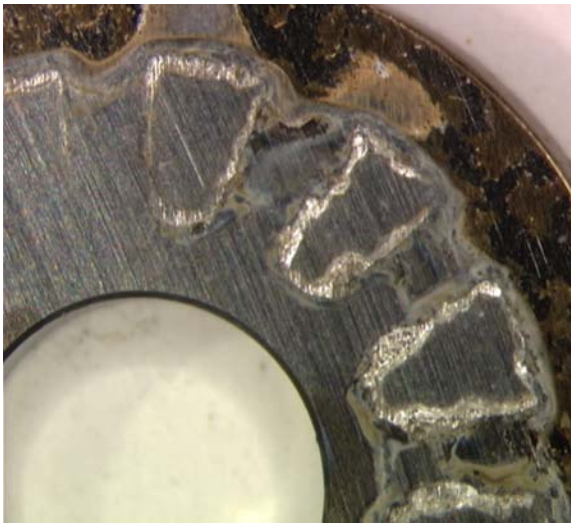

Figure 4.11– Specimen JE3328, MA polished Alloy 22 after CPP in 1 M NaCl at 90ºC

FIGURE 4.12 – Specimen JE3303, SHT Alloy 22 after CPP in 1 M NaCl at 90ºC

FIGURE 4.13 – Specimen JE3315, MA Alloy 22 after CPP in 6 m NaCl + 0.3 m KNO_3 at 100ºC

Figure 4.14 – Specimen JE3308, SHT Alloy 22 after CPP in 6 m NaCl + 0.3 m KNO_3 at 100ºC

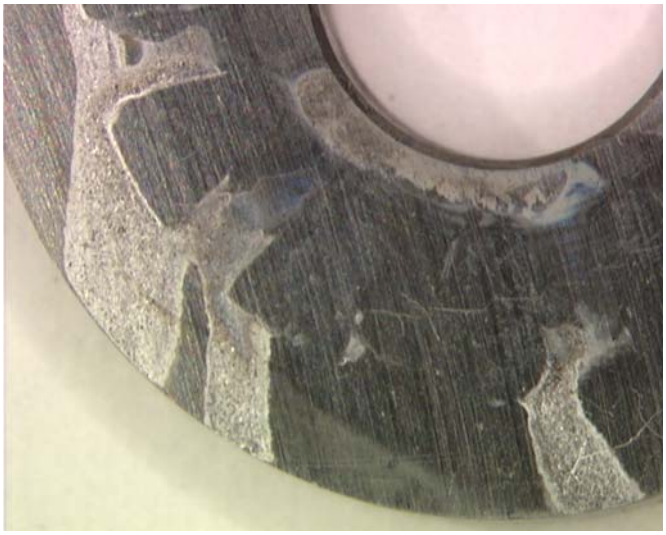

FIGURE 4.15 – Specimen JE3376, MA polished Alloy 22 after CPP in 5 M $CaCl_2$ at 90ºC

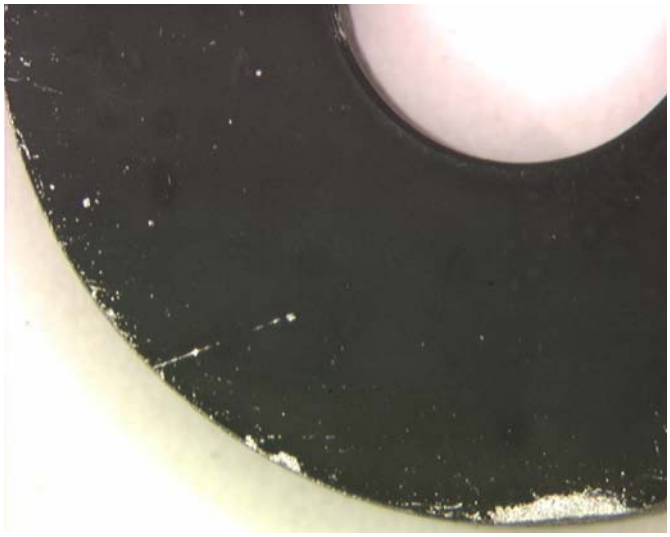

Figure 4.16 – Specimen JE3370, SHT Alloy 22 after CPP in 5 M $CaCl_2$ at 90ºC

Figure 4.17 – Specimen JE3381, MA polished Alloy 22 after CPP in 0.1 m NaCl + 0.001 m $NaHCO_3$ at 95ºC

Figure 4.18 – Specimen JE3373, SHT Alloy 22 after CPP in 0.1 m NaCl + 0.001 m $NaHCO_3$ at 95ºC

Figure 4.19 – Specimen JE3380, MA polished Alloy 22 after CPP in 0.1 m NaCl + 0.001 m $NaHCO_3$ at 60ºC

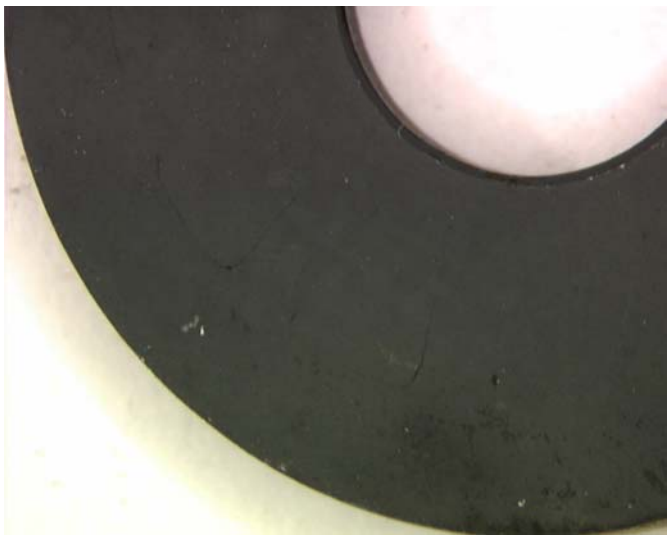

Figure 4.20 – Specimen JE3372, SHT Alloy 22 after CPP in 0.1 m NaCl + 0.001 m $NaHCO_3$ at 60ºC

5. Effect of Heat To Heat Variability on Corrosion of Ni-Cr-Mo Alloy Welds

5.1. Introduction

The effect of heat-to-heat variability was studied under the FY04 technical work plan (TWP) AWPT26. The results reported here pertain only to immersion corrosion tests. The electrochemical tests have not been performed yet. Testing was directed by John C. Estill and Tammy Summers. The tests were carried out by David V. Fix. The experimental details of this work are documented in SN-LLNL-SCI-483-V1, pages 78-139. The data is in TDMS under DTN LL050502512251.145.

The composition of engineering alloys such as Alloy 22 (N06022) and 686 (N06686) is given by ASTM standards (B 575). [1] When the alloys are commercially produced their chemical composition can vary slightly from heat to heat while still within the boundaries of the standard specification.

The fabrication history of the original welded plates is given elsewhere. [2-3] Basically, wrought plates with seven different heats (A through G) of Alloy 22 (Table 5.1 in Appendix 5.A) were welded with weld wire from seven different heats (1 through 7) of Alloy 686 (Table 5.2 in Appendix 5.A). The Alloy 22 plates were nominally 1-inch thick. The Alloy 686 or ERNiCrMo-14 weld wire was 0.0625-inch diameter and met the specifications of ASME SFA-5.14. [4] The welding method was gas tungsten arc welding (GTAW). Welded specimens from these 49 resulting plates were studied both in the as-welded (ASW) condition and in the solution heat-treated (SHT) (annealed) condition. The solution heat treating or annealing was carried in air at 2075°F for 1 h plus rapid cooling (water spraying). [2-3] Immersion corrosion tests were carried out in a boiling solution of sulfuric acid and ferric sulfate (ASTM G 28 A). [5]

The objective of this study is to show if small variations in the heat chemistry can affect the corrosion performance of Alloy 22 and Alloy 686.

Keywords: N06022, N06686, Heat Composition Variability, Corrosion Rate, ASTM G 28A

5.2. Experimental

5.2.1. Preparation of the Corrosion Coupons

The test material was delivered to Lawrence Livermore National Laboratory in the form of 1-inch thick welded plates. There were two types of plate strips: (1) As-Welded (ASW) and (2) ASW plus solution heat-treated (SHT). The welding and heat treatment were carried out in the primary metal producer plant. [2-3] Table 5.3 (Appendix 5.A) shows the identification of the coupons prepared from the welded plates. These plates were water-jet cut perpendicularly to the weld in approximately 1-inch thick slices. Then, the test coupons were abrasion wheel cut to immersion corrosion testing sizes from the plate slices. Each coupon contained the weld seam on

its center and base material at each side of the weld seam. The testing coupons were approximately 0.5 to 1-inch wide, 0.25 to 0.5-inch thick and 2-inch long. These sizes were constrained by the testing apparatus (ASTM G 28) and specimen holder. [5] That is, each coupon had six surfaces. Five of the surfaces were as-cut surfaces (abrasion wheel of water jet) and one surface (top surface) had the mill finish condition. In the case of the ASW + SHT coupons the top surface had also the characteristic black annealing oxide scale. A second batch of coupons were cut from the second "layer" of the plate, that is, the second batch did not contain the original weld surface or the SHT black oxide film on it (See SN-LLNL-483-V1 p. 102 for details).

The surface area of the coupons varied generally from 20 to 35 cm² and the weight in the varied from 30 to 60 g. The coupons were degreased in acetone, rinsed in de-ionized water and let dry in ambient air. Each coupon was labeled, photographed, dimensioned and then weighed three times before the corrosion testing started. At least 200 immersion tests were carried out in this work package.

5.2.2. Immersion Corrosion Tests (ASTM G28 A)

ASTM G 28 A method measures the susceptibility of nickel alloys to intergranular attack. It is often used to determine preferential intergranular attack near welds or in heat affected zones (HAZ). The guidelines are specified in the Annual Book of ASTM standards. [5] Figure 5.1 shows the setting for the tests. The ASTM G 28 A method for Alloy 22 consists in immersing coupons of the alloy for 24 h in a boiling solution of 42 g/L $Fe_2(SO_4)_3$ (ferric sulfate) plus 50% H_2SO_4 (sulfuric acid). This is a highly acidic and oxidizing solution. The difference in the mass of the coupon between before and after the test can be used to calculate the uniform corrosion rate (Equation 5.1) [5]

$$CR\left(\frac{mm}{year}\right) = \frac{8.76\times10^{4}\cdot\left(W_i - W_f\right)(g)}{A\left(cm^2\right)\cdot t(h)\cdot d\left(g\cdot cm^{-3}\right)} \qquad (5.1)$$

Where Wi is the initial mass of the coupon, Wf is the mass of the coupon after the 24-h immersion test, A is the surface area of the coupon, t is the testing time (24 h) and d is the density of Alloy 22 (8.69 g/cm³). [5] Only one coupon was tested for each base-weld combination.

Figure 5.1 - Set-up for immersion corrosion testing

5.3. Results

5.3.1. Corrosion Coupons Prepared from the Top Layer of the Plates

Figure 5.2 shows the general appearance of the top face of ASW 28R5 coupon, before and after the immersion test. Coupon 28R5 corresponded to Base Heat G welded with Wire Heat 7 (Table 5.3). Before the test, the coupon had a slight heat tint in the heat affected zone (HAZ) area. After the test, the HAZ appeared darker than the rest of the coupon, suggesting enhanced attack in this area. This can be seen as two darker bands at each side and parallel to the weld seam (Figure 5.2). The corrosion in the HAZ was mainly intergranular attack (IGA).

Figure 5.3 shows the general appearance of the top face of the ASW + SHT 73R5 coupon. Before the immersion test, the coupon was covered by a dark (black + dark green) oxide scale produced during the solution annealing and the subsequent water quenching. After the immersion test, most of the oxide scale was washed away and only the weld seam contained remnants of this scale. Many times there were islands of uneven attack in the weld seam within the area covered by the scale. In some weld seams, cavities were found. It is not clear if these cavities were formed during the immersion tests or were weld porosity formed during welding. The black HAZ bands of IGA present in the ASW coupons (Figure 5.2) were absent in the ASW + SHT coupons (Figure 5.3).

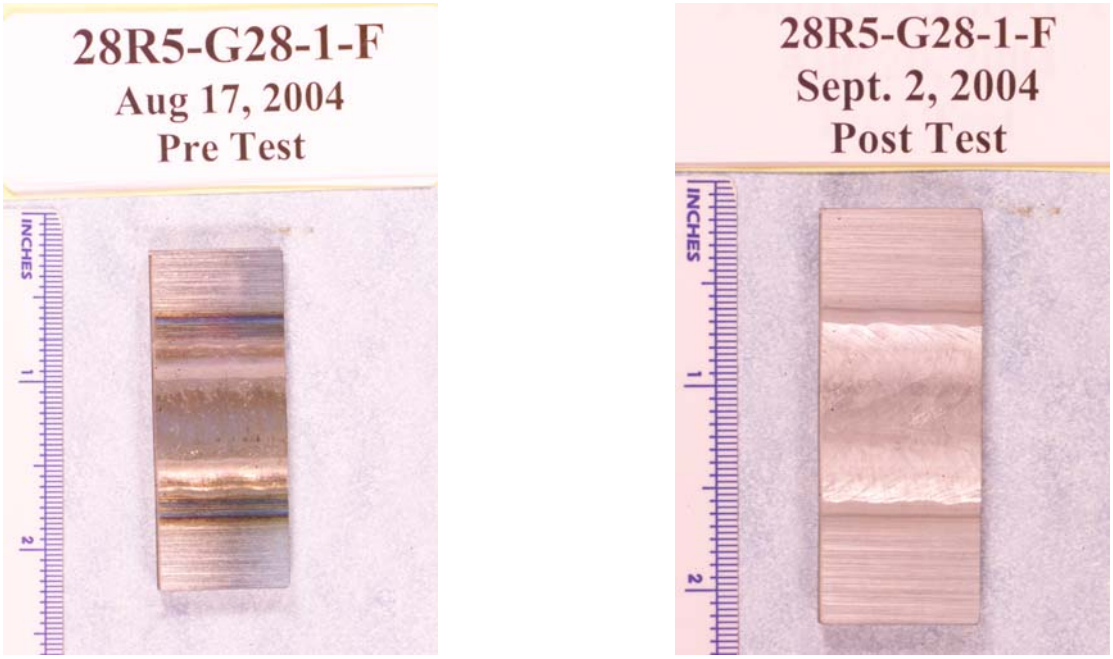

Figure 5.2. ASW Coupon 28R5 before (left) and after (right) the immersion test

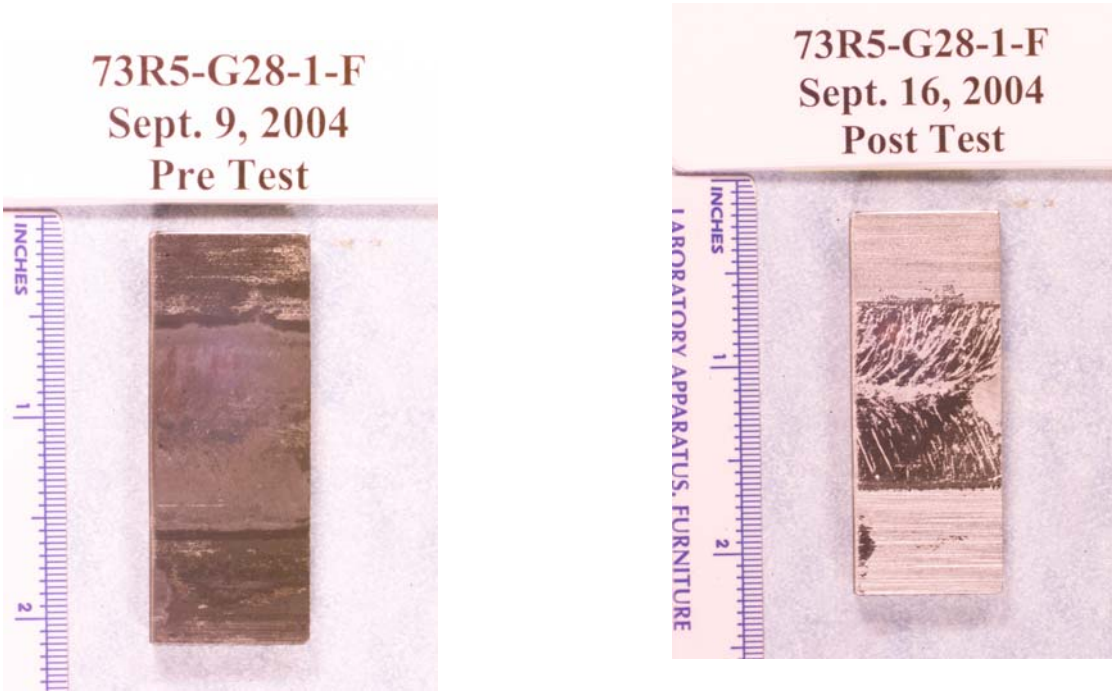

Figure 5.3. ASW + SHT Coupon 73R5 before (left) and after (right) the immersion test

Table 5.4 shows the corrosion rate results from the immersion testing. Figure 5.4 shows the corrosion rate for all the ASW coupons. Corrosion rate data are single values for each base-weld wire chemistry combination. Nonetheless, it is apparent from Figure 5.4 that the corrosion rate for most plate-weld wire pairs was between 0.8 and 1.2 mm/year. The corrosion rate of wrought and welded Alloy 22 from the literature and factory data is approximately 1 mm/year (40 mpy). [6-11] Figure 5.4 shows that there were a few coupons in the middle of the graph that had slightly higher corrosion rates. These coupons were prepared using Weld Wire 4 and base metal with "rich" chemistry (Heats E, F and G) (Table 5.1). It is likely that the rich chemistries accelerated the precipitation of deleterious ordered phases during welding, which later increased the corrosion rate of the coupons in the HAZ.

Figure 5.5 shows the corrosion rates for the ASW + SHT coupons. Figure 5.6 shows comparatively the corrosion rates for the ASW coupons (Figure 5.4) and the ASW + SHT coupons (Figure 5.5). In general the corrosion rates of the ASW + SHT coupons were higher than for the ASW coupons (Figure 5.4), probably because of the dissolution (or detachment) of the oxide scale from the top surface of the ASW + SHT coupons (Figure 5.3). Also, the testing electrolyte was darker after the tests for the ASW + SHT coupons than for the ASW coupons, suggesting more contamination of the electrolyte in the case of the ASW + SHT coupons. Mori et al. have shown that the corrosion rate of Ni- Cr-Mo alloys in ASTM G 28 solutions is highly dependent on the surface finish of the coupons. [12] Figure 5.5 shows that the corrosion rate of the ASW + SHT coupons seemed to increase for higher number weld wire heats. The higher number weld wire heats correspond to "richer" chemistries (Table 5.2), that is, the material that contained the highest amounts of Cr, Mo and W. Again, similarly to the data for ASW coupons (Figure 5.4), the ASW + SHT coupons welded with Wire 4 had higher than expected corrosion rates.

It has been reported previously that the Base Heat G did not meet the elongation to failure, required for wrought N06022 material, during mechanical testing. [2-3] Weldments produced using Wire 4 produced poor mechanical properties of the material (e.g. reduced tensile strength and low elongation to failure). [2-3] Poor mechanical properties of welded plates were also reported using wires 4 and 7 with plate D. [2-3] For most of the welded plates, a SHT process increased the Charpy toughness of the materials. The toughness of the welded coupons, both ASW and SHT were the lowest for the E, F and G plates welded with wire 4. [2-3] The poor performance of weld Wire 4 was attributed to the high content of residual elements. [2-3] These residual elements include Fe, Mn, V, Cu, Si and C (Table 5.2 in Appendix 5.A).

5.3.2. Corrosion Coupons Prepared from the Second Layer of the Plates

Figures 5.7 and 5.8 show the corrosion rates for coupons prepared from the second layer of the ASW and ASW + SHT plates, respectively. Compared to Figures 5.4 and 5.5 (top layer), the corrosion rates of the second layer coupons were lower, between 0.7 and 1 mm/year both for the ASW and ASW + SHT coupons. Figure 5.9 shows the corrosion rate for ASW and ASW + SHT coupons prepared from the second layer. There is very little difference in the corrosion rate of these two types of materials when the corrosion rate is not interfered by the external scale of the plate. Figure 5.9 seems to suggest that the corrosion rate of ASW + SHT coupons was slightly lower than that of ASW coupons, showing the beneficial effect of SHT. Figures 5.10 and

5.11 compare the corrosion rate for the top and second layer coupons for ASW and ASW + SHT coupons, respectively. In both cases, the corrosion rate of the second layer coupons was lower but this difference was larger for the ASW + SHT coupons since it contained a thicker oxide scale on the surface. In both cases it can be seen that coupons welded with Weld Wire 4 gave higher corrosion rates. Figures 5.12 and 5.13 show the appearance of the ASW and ASW + SHT coupons, respectively from the second layer before and after the corrosion immersion tests. Both coupons show the etching of the weld after the immersion tests. In most cases the weld etching was less conspicuous in the ASW + SHT specimens than in the ASW specimens. Figure 5.12 shows the black bands of HAZ IGA at both sides of the weld while these bands are absent in Figure 5.13 suggesting a beneficial effect of SHT. In many of the corrosion tested coupons there were corrosion pits in the fusion line of the weld. Also some coupons showed cracks and apparent corrosion between passes of the weld. This latter attack does not seem to be conspicuous enough to be manifested as higher corrosion rates (Figures 5.4 though 5.11).

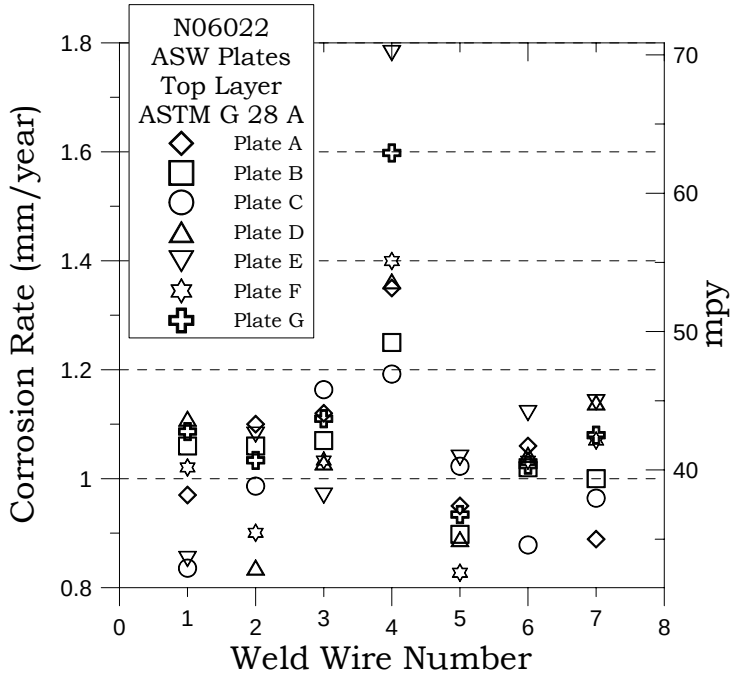

Figure 5.4. Corrosion Rates for Top-Layer ASW coupons

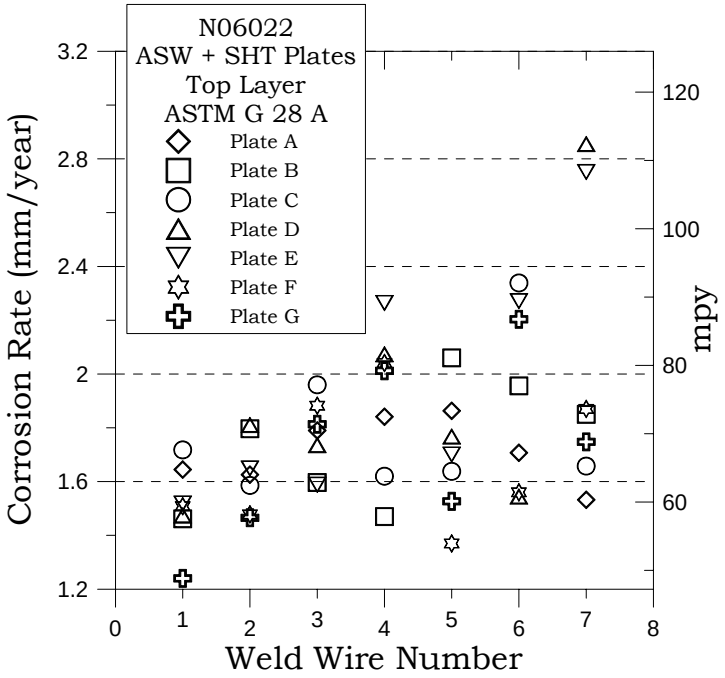

Figure 5.5. Corrosion Rates for Top-Layer ASW + SHT coupons

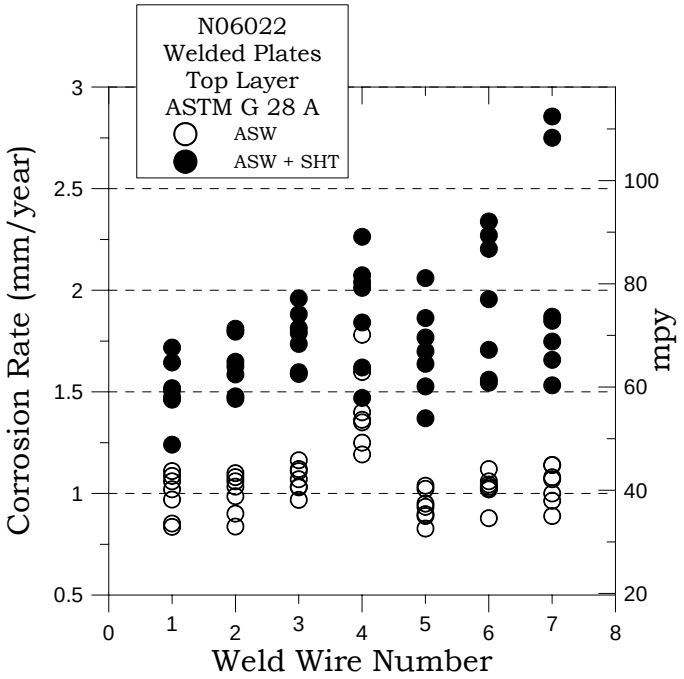

Figure 5.6. Corrosion Rates for Top-Layer ASW and ASW + SHT coupons

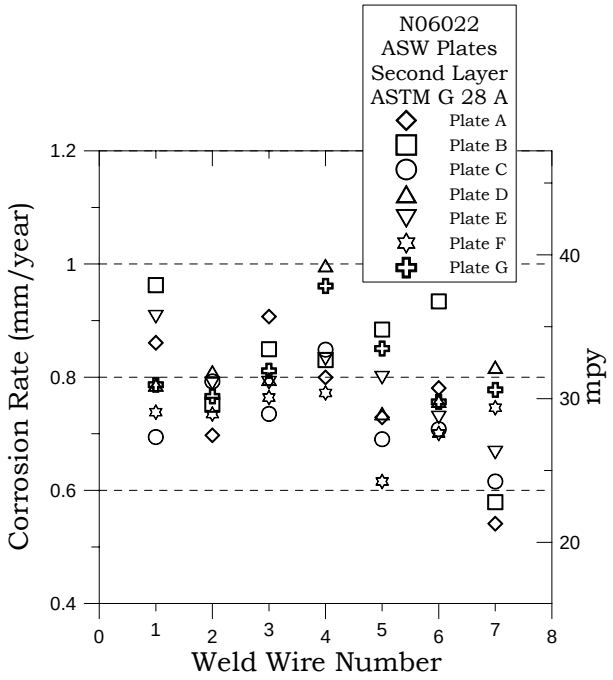

Figure 5.7. Corrosion Rates for Second-Layer ASW coupons

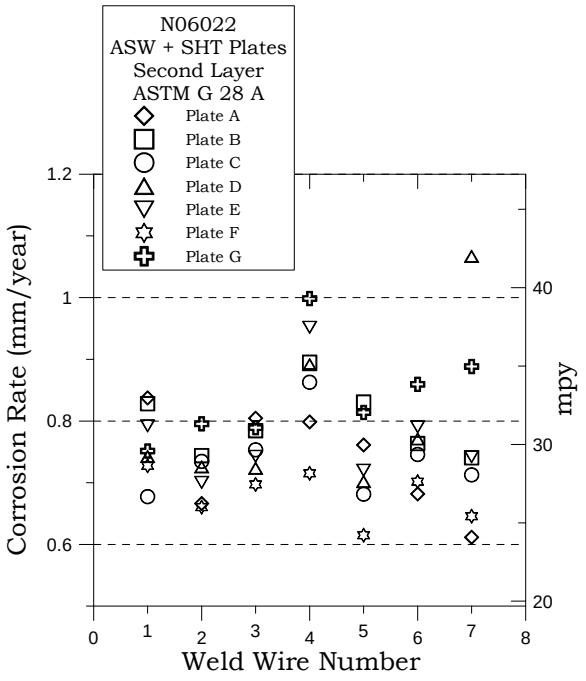

Figure 5.8. Corrosion Rates for Second-Layer ASW + SHT coupons

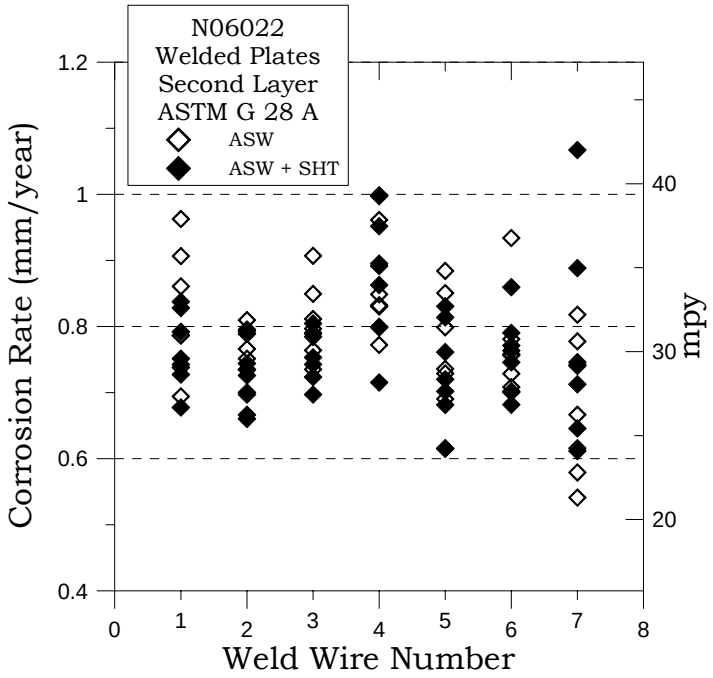

Figure 5.9. Corrosion Rates for Second-Layer ASW and ASW + SHT coupons

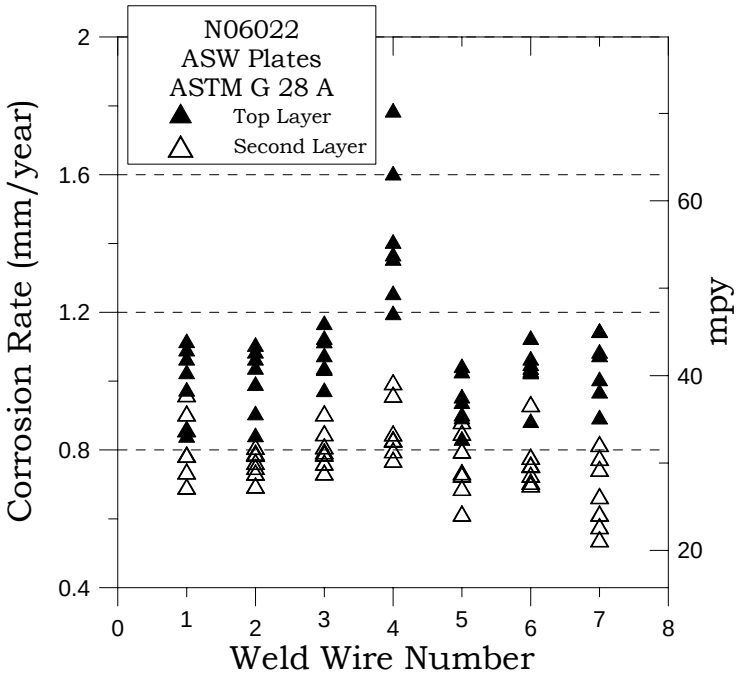

Figure 5.10. Corrosion Rates for Top and Second-Layer ASW coupons

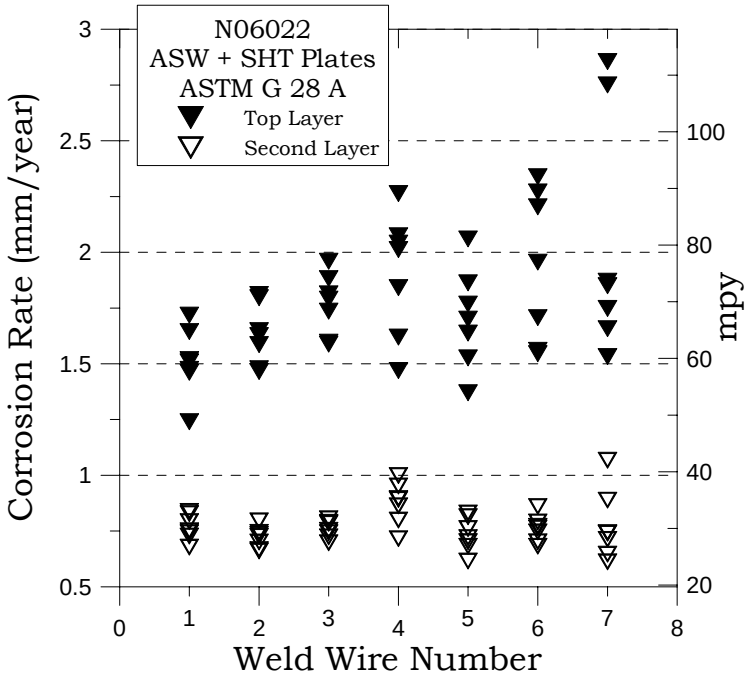

Figure 5.11. Corrosion Rates for Top and Second-Layer ASW + SHT coupons

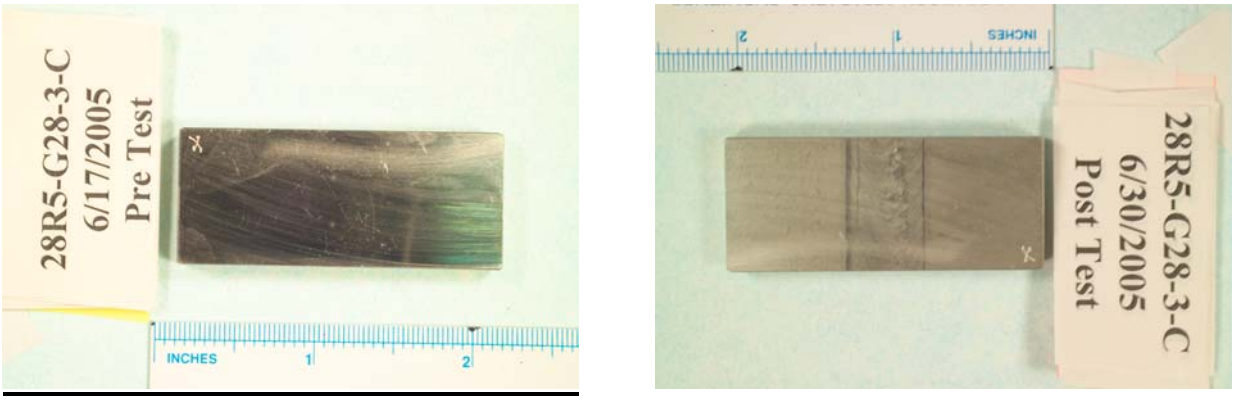

Figure 5.12. Coupon 28R5 from the Second Layer ASW plate
(Before and After the Tests)

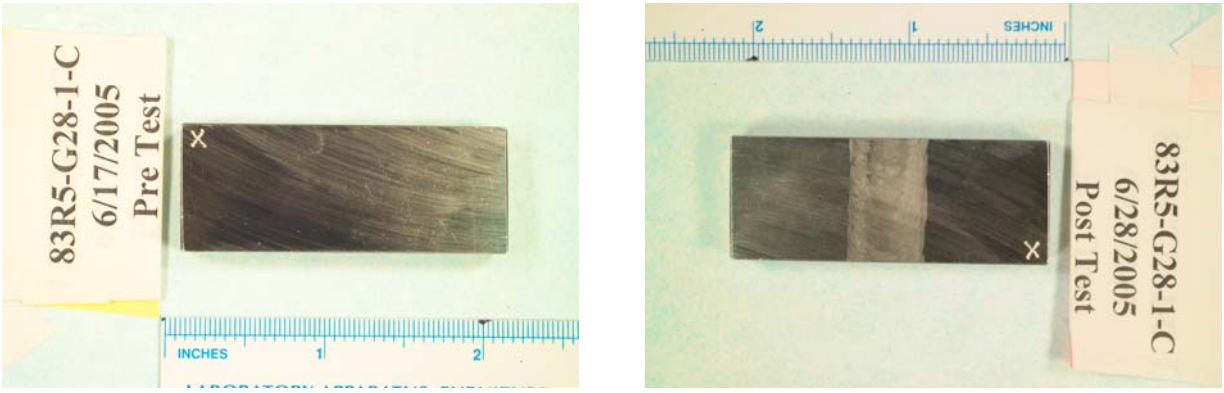

Figure 5.13. Coupon 83R5 from the Second Layer ASW + SHT plate (Before and After the Tests)

5.3.3. Final Remarks on Heat to Heat Variability

Results from the current testing shows that variations in the chemistry of both Alloy 22 and Alloy 686 within the range provided by the guiding standards do not affect the corrosion performance of these alloys. This is not surprising since when a primary metal producer develops and patents a new alloy, many different chemical compositions of the developed alloy are tested both for mechanical properties and for corrosion resistance in several types of electrolytes, generally from acidic reducing to acidic oxidizing. Later, the ranges of the chemical composition that give the desirable mechanical and corrosion properties are written into the standards which are presented to and accepted by societies such as ASTM of ASME. That is, the fact that the current test program failed to detect a change in the corrosion resistance of the alloys when their composition is varied within the margins of the approved standard could have been predicted based on the industrial experience. Even though some rich chemical compositions (when all important alloying elements such as Cr, Mo and W are at their maximum allowed concentration) gave slightly different behavior, it is unlikely that a commercial heat will have the maximum content of all the important elements, purely for economical reasons.

5.4. Conclusions

1. Corrosion rate of as-welded coupons of Alloy 22 plates with Alloy 686 wires in ASTM G 28 A solution were comparable to published data and in the order of 1 mm/year (40 mpy)
2. The corrosion rate of welded plus solution heat treated (ASW + SHT) coupons were higher than for ASW coupons, because the former contained an oxide scale in the surface that disintegrated during corrosion testing

3. When coupons were prepared from the second layer of the plates (without oxide scale on the surface) the corrosion rates of the ASW and the ASW + SHT coupons were similar.
4. In the range of the accepted chemistry of commercial materials the corrosion rate of one heat usually is indistinguishable from the corrosion rate of another heat.

5.5. References

1. ASTM International, Annual Book of ASTM Standards, Volume 02.04 "Non-Ferrous Metals" Standard B-575 (West Conshohocken, PA: ASTM International, 2004).
2. Allegheny Technologies, Report on "Nickel-Based Alloy Weld Filler Material and Base Metal Composition Test Program', Report 004223-REV 000, March 2004 (Allegheny Technologies, 2004: Albany, OR).
3. Waste Package and Drip Shield Corrosion, Technical Basis Document N° 6, Appendix T "Microstructural and Compositional Variations of Alloy 22," June 2004 (BSC, 2004: Las Vegas, NV)
4. ASME (American Society of Mechanical Engineers), 2001 ASME Boiler and Pressure Vessel Code (ASME, 2001: New York, NY).
5. ASTM International, Annual Book of ASTM Standards, Volume 03.02 "Wear and Erosion; Metal Corrosion" p. 91 (West Conshohocken, PA: ASTM International, 2004).
6. Haynes International Inc., "Hastelloy C-22 Alloy," Product Brochure H-2019E (1997).
7. R. B. Rebak and N. E. Koon, Corrosion/1998, Paper 153 (NACE International, 1998: Houston, TX).
8. R. B. Rebak, N. E. Koon, J. R. Dillman, P. Crook and T. S. E. Summers, Corrosion/2000, Paper 00181 (NACE International, 2000: Houston, TX).
9. R. B. Rebak, T. S. E. Summers, T. Lian, R. M. Carranza, J. R. Dillman, T. Corbin and P. Crook "Effect of Thermal Aging on the Corrosion Behavior of Wrought and Welded Alloy 22," Corrosion/2002, Paper 02542 (NACE International, 2002: Houston, TX).
10. R. B. Rebak and P. Crook, PVP-Vol. 449, p. 111 (ASME, 2002: New York, NY).
11. R. B. Rebak, ASM Metals Handbook, Vol. 13A, p. 279 (ASM International, 2003, Metals Park, OH).
12. G. Mori, S. Sutthiruangwong, M. Czerny and T. Partlic, Corrosion, 60, 1082 (2004).
13. R. B. Rebak and P. Crook, PVP-Vol. 483, p. 131 (ASME, 2004: New York, NY).

APPENDIX 5.A

Table 5.1. Approximate Average Chemical Composition of the N06022 Plates (Heats A-G)

Element ↓ Heat →	**A**	**B**	**C**	**D**	**E**	**F**	**G**
Ni	61.6	59.6	58.5	56.00	56.3	58.1	53.9
Cr	20.3	20.8	21.1	21.3	21.6	21.8	22.5
Mo	12.7	13.3	13.1	13.6	13.7	13.8	14.2
W	2.7	3.0	3.0	3.0	3.0	3.0	3.4
Fe	2.5	3.0	4.0	3.0	5.0	3.0	5.8
Co	0.15	ND	ND	2.23	ND	0.03	ND
Mn	0.02	0.02	0.01	0.4	0.04	0.02	0.03
Al	0.18	0.15	0.17	0.15	0.15	0.19	0.20
V	ND	ND	ND	0.25	0.01	0.01	0.01
Cu	0.01	0.01	ND	0.02	ND	0.01	ND
Si	0.03	0.03	0.03	0.07	0.04	0.05	0.05
C	0.004	0.004	0.006	0.005	0.01	0.014	0.007
S	0.0003	ND	ND	ND	ND	ND	ND
P	0.003	0.004	0.004	ND	0.006	0.005	0.006
ND = Not Detected (Below the Detection Limit)							

Table 5.2. Approximate Average Chemical Composition of the N06686 Weld Wires (Heats 1-7)

Element ↓ Heat →	**1**	**2**	**3**	**4**	**5**	**6**	**7**
Ni	61.9	60.4	58.8	53.6	57.8	56.8	55.6
Cr	19.3	19.8	20.5	20.6	21.6	22.3	22.9
Mo	15.1	15.8	16.3	16.3	16.3	16.3	16.8
W	3.2	3.5	3.7	3.8	3.8	4.0	4.3
Fe	ND	0.42	0.39	4.03	0.28	0.35	0.14
Co	ND	ND	ND	0.02	ND	ND	ND
Mn	ND	ND	ND	0.89	ND	ND	ND
Al	0.15	0.16	0.17	0.06	0.18	0.16	0.16
V	ND	ND	ND	0.11	ND	ND	ND
Cu	ND	0.01	0.01	0.43	0.01	0.01	0.01
Si	0.02	0.02	0.03	0.08	0.02	0.03	0.03
C	0.004	0.005	0.002	0.005	0.001	0.001	0.002
S	ND	ND	ND	ND	ND	ND	ND
P	ND	0.006	0.007	ND	0.008	0.008	0.01
ND = Not Detected (Below the Detection Limit)							

Table 5.3. Welded Plates Designation Based on the Chemistry of Base Plate and Weld Wire

Chemistry of Base and Weld	ASW Plate ID	ASW + SHT Plate ID		Chemistry of Base and Weld	ASW Plate ID	ASW + SHT Plate ID
A1	4R5	5R5		E1	8R5	9R5
A2	14R5	15R5		E2	18R5	19R5
A3	64R5	65R5		E3	70R5	71R5
A4	84R5	85R5		E4	190R5	91R5
A5	42R5	43R5		E5	46R5	47R5
A6	50R5	51R5		E6	58R5	59R5
A7	30R5	31R5		E7	34R5	135R5
B1	6R5	7R5		F1	2R5	3R5
B2	17R5	16R5		F2	12R5	13R5
B3	66R5	67R5		F3	72R5	73R5
B4	82R5	83R5		F4	88R5	89R5
B5	44R5	45R5		F5	38R5	39R5
B6	56R5	57R5		F6	54R5	55R5
B7	32R5	33R5		F7	26R5	127R5
C1	10R5	11R5		G1	24R5	25R5
C2	120R5	21R5		G2	122R5	23R5
C3	168R5	69R5		G3	162R5	63R5
C4	92R5	93R5		G4	98R5	99R5
C5	148R5	49R5		G5	40R5	41R5
C6	60R5	61R5		G6	52R5	53R5
C7	36R5	37R5		G7	28R5	29R5
D1	94R5	95R5				
D2	96R5	97R5				
D3	80R5	81R5				
D4	86R5	87R5				
D5	78R5	79R5				
D6	74R5	75R5				
D7	176R5	177R5				

Table 5.4. Corrosion Rate in ASTM G 28A of Coupons Prepared from the Top of the Welded Plates

ASW Plate ID	Corrosion Rate (mm/year)	ASW + SHT Plate ID	Corrosion Rate (mm/year)		ASW Plate ID	Corrosion Rate (mm/year)	ASW + SHT Plate ID	Corrosion Rate (mm/year)
4R5	0.97	5R5	1.64		8R5	0.85	9R5	1.52
14R5	1.10	15R5	1.63		18R5	1.08	19R5	1.65
64R5	1.12	65R5	1.79		70R5	0.97	71R5	1.59
84R5	1.35	85R5	1.84		190R5	1.78	91R5	2.26
42R5	0.95	43R5	1.86		46R5	1.04	47R5	1.70
50R5	1.06	51R5	1.71		58R5	1.12	59R5	2.27
30R5	0.89	31R5	1.53		34R5	1.14	135R5	2.75
6R5	1.06	7R5	1.46		2R5	1.02	3R5	1.51
17R5	1.06	16R5	1.80		12R5	0.90	13R5	1.48
66R5	1.07	67R5	1.60		72R5	1.03	73R5	1.88
82R5	1.25	83R5	1.47		88R5	1.40	89R5	2.04
44R5	0.90	45R5	2.06		38R5	0.83	39R5	1.37
56R5	1.02	57R5	1.96		54R5	1.03	55R5	1.56
32R5	1.00	33R5	1.85		26R5	1.07	127R5	1.87
10R5	0.84	11R5	1.72		24R5	1.09	25R5	1.24
120R5	0.99	21R5	1.59		122R5	1.03	23R5	1.47
168R5	1.16	69R5	1.96		162R5	1.11	63R5	1.81
92R5	1.19	93R5	1.62		98R5	1.60	99R5	2.01
148R5	1.02	49R5	1.64		40R5	0.93	41R5	1.53
60R5	0.88	61R5	2.34		52R5	1.02	53R5	2.20
36R5	0.96	37R5	1.66		28R5	1.08	29R5	1.75
94R5	1.11	95R5	1.47					
96R5	0.84	97R5	1.81					
80R5	1.03	81R5	1.74					
86R5	1.36	87R5	2.07					
78R5	0.89	79R5	1.77					
74R5	1.04	75R5	1.54					
176R5	1.14	177R5	2.86					
The top layer corresponds to the coupons that had the original surface of the welded plates								